ALMA MATER STUDIORUM · UNIVERSITÀ DI BOLOGNA

Scuola di Scienze
Dipartimento di Fisica e Astronomia
Corso di Laurea Magistrale in Fisica

Isospin transport phenomena in nuclear reactions in the Fermi energy range

Relatore:
Prof. Mauro Bruno

Correlatore:
Dott. Chbihi Abdelouahad

Prof. Gianni Vannini

Presentata da:
Simone Velardita

Anno Accademico 2018/2019

Abstract

This thesis work has been done within the NUCL-EX group of the INFN group II. The work has consisted of the preparation and the first measurement of the coupled apparatus INDRA-FAZIA, in the identification of data obtained in the previous measurement with FAZIA and in the analysis of data that were already calibrated in a precedent measurement with the apparatus INDRA coupled with the spectrometer VAMOS. The INDRA apparatus is a device that has been in operation for many years and is still fully functional and that at the time of construction was one of the most modern apparatuses. The FAZIA apparatus was built with a collaboration that involves more than 10 institutions in the field of nuclear physics in six different countries, but mainly with Italian-French leadership. A long phase of research and development was necessary to obtain what today can be considered one of the best apparatus for measurements of charged particles emitted in nuclear reactions that allows a great resolution in charge and mass of the particles, besides the measurement of their energy with great precision and great energy range.

The measurement made with INDRA-VAMOS was analyzed in order to verify the isospin effects (N/Z content) in peripheral and semi-peripheral reactions $^{40,48}Ca +^{40,48} Ca$ at $35\,MeV/u$. In these collisions, the transport models predict the formation of a low-density neck between two hot fragments kinematically similar to the projectile (*Projectile-Like Fragment*, PLF) and target (*Target-Like Fragment*, TLF). The isotopic identification of PLF provided by VAMOS, together with those of *light charged particles* (LCP) revealed in coincidence with INDRA allow, through their correlation, to reconstruct the primary fragment. During the reconstruction phase, the mass number

(A) is made without the emitted neutron contribution, because these are not detected. To estimate the excitation of the source is necessary to make some assumption about the evaporated neutrons, to obtain the most realistic estimate. Finally, in order to extrapolate information about the energy symmetry term of the Nuclear Equation of State, it is shown the study of the width of isotopic distributions. The preliminary result obtained is the trend of the symmetry energy coefficient (C_{sym}) as a function of the charge of the reconstructed primary fragment, which is dependent on the surface term, present in the liquid drop model of the nucleus. However, require further investigation before drawing a definitive conclusion.

Confirmations and further information on the isospin transport can be obtained with the analyzes of the measurements that have been made with the apparatus INDRA and FAZIA.

Sommario

Questo lavoro di tesi è stato svolto nell'ambito del gruppo NUCL-EX del gruppo II dell'INFN. Il lavoro è consistito nell'allestimento e le prime misure degli apparati accoppiati FAZIA e INDRA, nell' identificazione di dati ottenuti in misure con l'apparato FAZIA e nella analisi di dati già calibrati ottenuti in misure precedenti con l'apparato INDRA accoppiato allo spettrometro VAMOS. L'apparato INDRA è un apparato in funzione da tanti anni e tuttora perfettamente funzionante e che all'epoca della costruzione era uno degli apparati piu' moderni. L'apparato FAZIA è stato costruito con una collaborazione che coinvolge più di 10 istituzioni nel campo della fisica nucleare in sei paesi diversi, ma principalmente a guida italo-francese. E' stata necessaria una lunga fase di ricerca e sviluppo per ottenere quello che al giorno d'oggi può essere considerato un apparato di punta per misure di particelle cariche emesse in reazioni nucleari che consente una grande risoluzione in carica e massa delle particelle, oltre alla misura della loro energia con grande precisione e grande intervallo energetico.

La misura effettuata con gli apparati INDRA e VAMOS è stata analizzata allo scopo di verificare gli effetti di isospin (contenuto N/Z) nelle reazioni periferiche e semiperiferiche $^{40,48}Ca +^{40,48} Ca$ a 35 MeV/u. Per queste collisioni i modelli di trasporto predicono la formazione di una regione (neck) a bassa densità tra due frammenti caldi che sono cinematicamente simili al proiettile (*Projectile-Like Fragment*, PLF) e al bersaglio (*Target-Like Fragment*, TLF). La correlazione tra l'identificazione isotopica dei PLF fornita da VAMOS e quella delle particelle cariche leggere (*Light Carged Particle*, LCP), rivelate in coincidenza con INDRA, permette di ricostruire il frammento primario. Nella fase di ricostruzione il numero di massa del frammento (A) non presenta

il contributo dei neutroni emessi, dato che questi non vengono rivelati. Per stimare l'energia d'eccitazione della sorgente sono state fatte delle assunzioni sul numero di neutroni evaporati in modo da avere una stima più realistica. Per poter estrapolare informazioni sul termine di energia di simmetria dell'equazione di stato nucleare è stato effettuato uno studio sulla larghezza delle distribuzioni isotopiche. Il risultato preliminare ottenuto è l'andamento del coefficiente dell'energia di simmetria (C_{sym}) in funzione della carica del primario ricostruito, che risulta dipendente dal termine di superficie, presente nel modello a goccia di liquido del nucleo. Tuttavia, richiede ulteriori studi prima di poter dare conclusioni definitive.

Conferme e ulteriori informazioni sul trasporto di isospin potranno essere ottenute con le analisi delle misure che sono state effettuate con gli apparati INDRA e FAZIA.

Contents

Introduction

The understanding of the strong interaction that binds protons and neutrons within the atomic nucleus is an issue that remains topical in nuclear physics. This effective interaction between the nucleons, in particular, determines the equation of state of a nuclear system and makes it possible to describe the structure of the nuclei, the properties of the neutron stars, the nucleosynthesis and the mechanisms of the explosion of the supernovae. Several constraints are now established on spherical nuclei, notably through adjustments between phenomenological nucleon-nucleon potentials and the masses of nuclei measured in the laboratory. Nevertheless, the predictions made by the models differ greatly as one moves away from the stability valley, the saturation density or symmetric nuclei (symmetry defined using the isospin, i.e. the ratio between the number of neutrons and protons of the nucleus). In particular, the description of the density dependence of the symmetric energy term, that is the energy cost of introducing asymmetry into isospin, is a major challenge of modern nuclear physics. Therefore laboratory heavy ion collisions are a unique means of subject nuclear systems to extreme conditions of pressure, density, temperature and isospin. The NUCL-EX collaboration has, in the lasts decade, focused its attention on this kind of physics, especially with the FAZIA project. The aim of the project is to build an array for charged particles, with high granularity and good energy resolution, with A and Z identification capability over the widest possible range.

This thesis is organized as follows. In Chapter 1 the general case of the nuclear reactions will be introduced with particular attention to the reaction mechanisms in the Fermi energy range. Then is introduced the Nuclear Equation of State and the observables sensitive to the energy symmetry term. Chapter 2 is dedicated to the FAZIA project, it is shown the main characteristics of the FAZIA detectors, its coupling with the 4π multi-detector INDRA performed at GANIL in 2019 and the last section is dedicated to its Identification techniques. In Chapter 3, we present the data of the previous INDRA-VAMOS campaign (*e503*) for the reactions $^{40,48}Ca + ^{40,48}Ca$ at 35 MeV/u, and the way we are able to reconstruct the primary fragment making the correlation between the light charged particles (LCP), detected in INDRA and the projectile like fragments (PLF), detected in VAMOS. In Chapter 4, we compare the obtained reconstruction to the model AMD (*Antisimmetrized Molecular Dynamics*) plus GEMINI++ (statistical decay code), using the first for the description of the dynamical phase and the second one as after-burner to simulate the de-exciting process which brings the initially excited fragments towards the ground or low-lying states. Then, it is shown the extrapolation of some observables such as the excitation energy and the temperature of the primary fragment. In the last part of the chapter the preliminary results of the energy symmetry term study are shown. Finally, conclusions and perspectives are drawn.

Chapter 1

Physical case

1.1 Heavy-ion collision

The behaviour of nuclear matter in several conditions of density, temperature and N/Z asymmetry is of fundamental importance for the understanding of many phenomena involving nuclear systems and astrophysical compact objects. This information can be accessed by means of heavy-ion collision experiments, where transient states of nuclear matter, which include a large variety of regimes, can be created.

We study the reaction mechanisms to classify collision according to some global topological features. In fact, each collision can mainly be related to the concept of *impact parameter* (b) and to the dissipation of the kinetic energy available in the center of mass of the projectile and the target in the form of *excitation energy* (E^*). This dissipation process is governed by several important ingredients. One of this is the relative velocity between the initial partners of the reaction v_{rel}, to which we can associate a reduced wavelength of the nucleon-nucleon collision, such that:

$$\lambdabar = \frac{\lambda}{2\pi} = \frac{\hbar}{m_u v_{rel}} \tag{1.1}$$

where $m_u = 1.66 \cdot 10^{-27}\, kg$ is the unit of atomic mass and $\hbar = h/2\pi$ with $h = 6.63 \cdot 10^{-34}\, m^2 \cdot kg \cdot s^{-1}$ the Planck constant.

The value of eq.(1.1) depends on the beam energy and we have to compare it with the mean nucleon-nucleon distance in a nucleus (typically 2 fm): if $\lambda\!\!\!^{-}$ exceeds this distance, a collective behaviour of nucleons is expected, i.e., the medium field effects (one body) predominate on the effects of the nucleon-nucleon (two-body) collisions; if $\lambda\!\!\!^{-}$ is smaller, conversely, a two-body collision is expected. In the former case, the energy is dissipated through the interaction of individual nucleons with the nuclear mean field with a thermalization time of the order

$$\tau_{1-body} \simeq \frac{R}{v_F} \tag{1.2}$$

in which R is of the order of the sum of two interacting nuclei radii and $v_F(\sim 0.3c)$ is the Fermi velocity. In the second case, the energy is dissipated through elastic nucleon-nucleon collisions and the associated thermalization time is of the order of the mean time between two successive nucleon-nucleon collisions which can be estimated from kinetic theory as:

$$\tau_{2-body} = \frac{1}{\sigma_{nn}\rho_0 v} \tag{1.3}$$

where σ_{nn} is the nucleon-nucleon cross section in the medium, v the mean velocity and ρ_0 the medium density.

Reaction mechanisms involved in nucleus-nucleus collisions have been extensively studied at low [2,3] ($< 15\,MeV/u$) and high [4,5] ($> 200\,MeV/u$) *incident energy* (E_{inc}, the energy per nucleon of the beam in the laboratory frame). In the low energy regime, in the Coulomb barrier region and below $15\,MeV/u$, according to the fig. (1.1) we can use the *orbital angular momentum* (ℓ), correlated to the impact parameter, in order to classify the different reaction mechanisms:

- *elastic scattering* for $\ell > \ell_{gr}$[1], where the distance between projectile and target nucleus is such that the nuclear force is completely negligible with respect to the Coulomb one;

- *quasi-elastic scattering* for $\ell_{DIC} < \ell < \ell_{gr}$, where the kinematics of the two nuclei

---

[1] Refers to the *grazing angle*, that corresponding to the trajectory for which the two nuclei just touch each other.

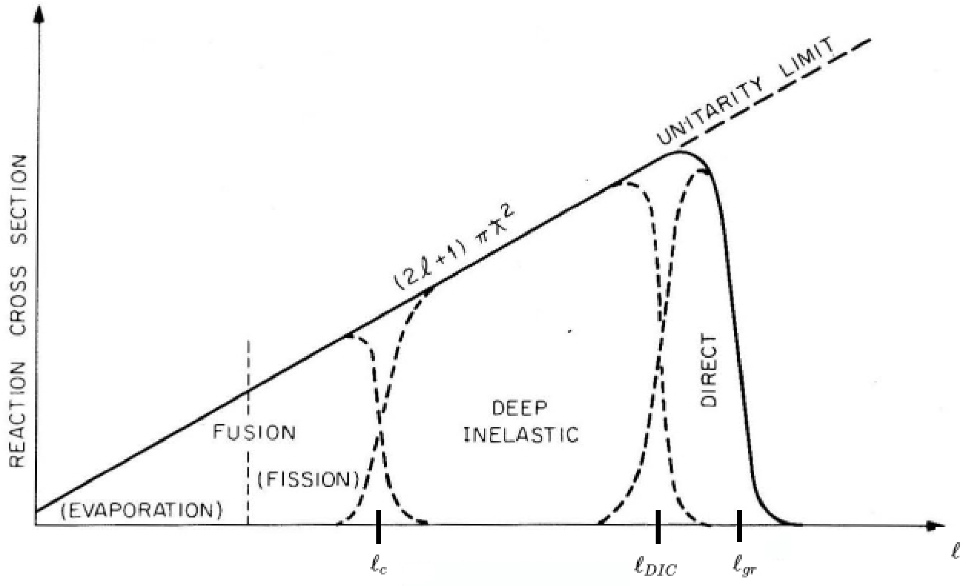

Figure 1.1: A schematic diagram of the partial wave decomposition of the reaction cross-section in low incident energy heavy-ion reactions: the abscissa refers to orbital angular momentum or to the impact parameter [1].

is just slightly perturbed and only few nucleon transfers between projectile and target are possible;

- *deep inelastic collision* (*DIC*) for $\ell_{crit} < \ell < \ell_{DIC}$, where the two partners re-separate after a contact phase during which matter and a significant part of the energy are exchanged;
- *central collision* for $\ell < \ell_{crit}$ (see fig.(1.2)), where the main process is the complete fusion with the creation of a *Compound Nucleus* (*CN*) with a total loss of the initial system memory.

In the high energy regime, $E_{inc} > 200\, MeV/u$, the collision is dominated by hadronic cascades because $\lambda\!\!\!^{-}$ associated is shorter than the nucleon-nucleon distance and the $v_{rel} > v_{Fermi}$. For these two reasons the description generally used is geometrical and is

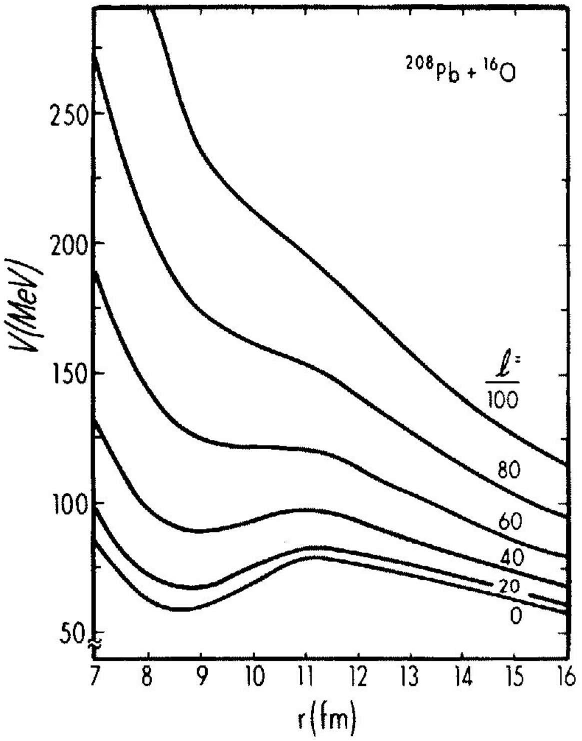

Figure 1.2: Evolution of the interaction potential between two interacting nuclei as a function of the relative distance r. The total potential including the nuclear, centrifugal and Coulomb contributions is shown for various values of the angular momentum ℓ . The critical angular momentum ℓ_{crit} corresponds to the ℓ value for which the pocket of the potential curve disappears (here around $\ell \sim 60$) [6].

called *participant-spectator picture*, see fig.(1.3) : nucleons which do not belong to the overlapping zone of the two incoming nuclei do not undergo nucleon-nucleon collisions and constitute the *spectators* while the other ones are the *participants*. The spectator anyhow can be excited at relatively low excitation energies.

In the context of this thesis, we are particularly interested in collisions of heavy ions in the Fermi energy regime and it will be described in the next section.

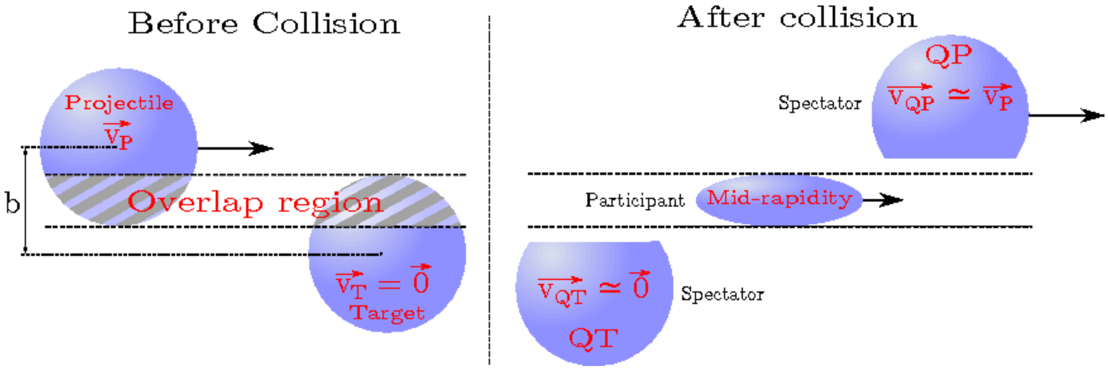

Figure 1.3: *Participant-spectator picture*

1.1.1 Reaction mechanisms to intermediate energies

The physics of nuclei colliding with intermediate energies, $15 < E_{inc} < 200\,(MeV/u)$, is at the junction of the two previous energy ranges, where the one and two body dissipation mechanisms compete.

Whatever the dissipation mechanisms, the thermalization time, eqq.(1.3,1.2), is comparable to the interaction time since this latter is of the order of

$$\tau_{int} = \frac{R}{v_{rel}} \tag{1.4}$$

in which R is of the order of the sum of the two interacting nuclei radii, and v_{rel} is the relative velocity between the two initial partners in the entrance channel of the reaction. From this fact one may assert two important conclusions:

- a fraction of the available energy can be thermalized during the interaction between the projectile and the target: it is then possible to create very hot fragment during nucleus-nucleus collisions at the Fermi energy domain;
- a fraction of the available energy can be not thermalized during the collision, which leads to a rapid emission before the thermalization. This emission is called *pre-equilibrium emission*.

However, part of the energy is also used to excite collective degrees of freedom associated with deformation, rotation and/or compression. The proportion of energy stored in a given mode depends on the typical timescales for the excitation of this mode and also on the initial conditions, i.e. the entrance channel characteristics. Indeed, we understand the importance of the impact parameter of the collision, since the dissipation energy and the deformation of the emitted nuclei are greater for lower impact parameter.

Central collisions For *central* we mean those collisions that are, in the whole energy range, characterized by the total fusion of the projectile and target which lead to the formation of a single fused system with excitation energy (E^*) comparable with the energy available in the center of mass of the reaction. Several mechanisms of de-excitation are distinguished according to the excitation reached by the system: **fission**, **evaporation** and **multifragmentation**, see fig. (1.4). For $E^* \leq 4\,MeV/u$ the description of the decay is close to that in the range of the Coulomb energies, i.e., the competition between fission and evaporation(statistical emission of particles by a single source in equilibrium). The competition of these two mechanisms makes it possible to better charaterize the fission and to experimentally estimate the associated time scales. Let us note that the evolution of the fission times as a function of the excitation energy makes it possible to better understand the nature (1 or 2-body) of the nuclear viscosity and to constrain its temperature dependence.

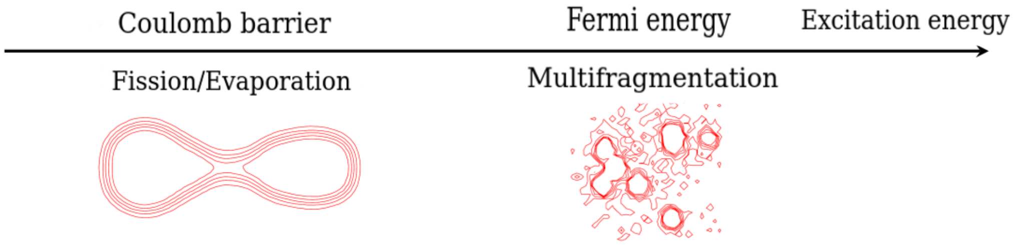

Figure 1.4: Schematic rappresentation of the de-excitation mechanism according to the excitation reached by the system.

By increasing the incident energy, the complete fusion gradually disappears until it is replaced by the incomplete fusion and the excitation energy increases. For $E^* > 4\,AMeV$ the multifragmentation mechanism becomes predominant ([7]). Multifragmentation is by definition the almost simultaneous production of several ($N_{frag} > 3$) fragments with $Z > 2$. This type of mechanism has been the subject of numerous investigations in recent years ([8–10]) because it makes it possible to study the phase diagram of nuclei.

Peripheral collisions This kind of collisions exhaust a large amount of the total cross-section. A general overview is accessible, using a bi-dimensional plot where the abscissa and ordinate are, respectively, the *parallel* to the beam ($v_{//}$) and *perpendicular* to the beam ($v_{\perp}$) velocity components. The variable in the third axis is the cross-section.

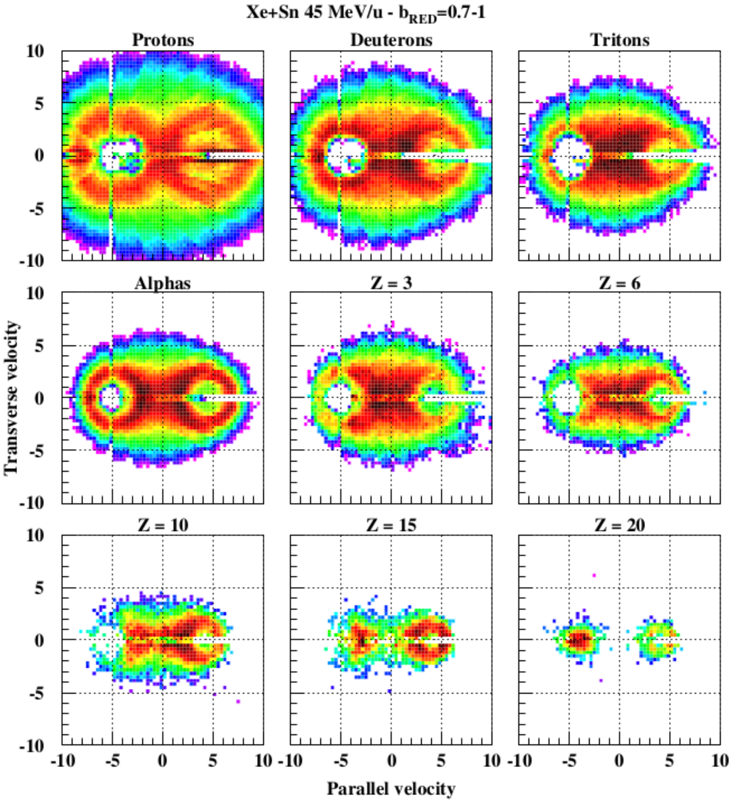

Figure 1.5: Iso-contour plots of $v_{//} - v_{\perp}$ (in cm/ns) for selected events observed in Xe+Sn collisions at 45 MeV/u for various emitted species from protons up to $Z = 20$. Events selected correspond to mid-central collisions [6].

In fig. (1.5), two sources of emission associated with circular contours (*Coulomb cir-*

cles) are seen, especially for protons, alphas and heavy fragments ($Z = 20$). This is a general result: in peripheral and mid-central collision, a *Quasi-Projectile* (**QP**) and a *Quasi-Target* (**QT**) are produced in the collision. If the decay chain is complicated or long the final products are quite different from the original QP and QT nuclei. On contrary, if it is simple or short, the QP and QT residues still resemble the initial projectile and target nuclei. However, there is an extra particle emission in between the two sources, the so-called *mid-rapidity zone*. This intermediate velocity zone is the origin of the emission of light charged particles (**LCP**, $Z = 1 - 2$) and intermediate mass fragments (**IMF**, $3 \leq Z \leq 10$), that has to be considered in addiction to the evaporation of the QP and QT. The two large final product are called, respectively, projectile-like and target-like fragments (**PLF** and **TLF**, respectively).

1.2 The nuclear equation of state

The nuclear equation of state (*EoS*) is a fundamental property of the nuclear matter. It describes the relationship between the energy, temperature, density and the ratio (*asymmetry*) neutron-proton also called *isospin*. Although several constraints have already been placed on the EoS for symmetric nuclear matter around the nuclear saturation density ρ_0 [11], the EoS for nuclear asymmetric matter is still subject of many questions. How to predict the interaction of nucleons in the medium in the case of a large neutron/proton asymmetry, a large temperature variation and/or when the density is far from ρ_0. In recent years, many theoretical and experimental efforts have been made to study the EoS for the asymmetric nuclear matter and in particular the *symmetry energy term* [12–20]. In this section, we describe the general properties of the asymmetry energy term and some observables related to the latter.

1.2.1 Liquid drop model

Historically the asymmetry energy term has appeared in the semi-empirical Bethe-Weizsacker formula, eq.(1.5), expressing the binding energy of a finite-sized nucleus consisting of N neutrons and Z protons [21].

The theory behind the formula is the liquid drop model proposed by George Gamow [22], which can account for most of the terms in the formula and gives rough estimates for the values of the coefficients. The liquid drop model treats the nucleus as a drop of incompressible nuclear fluid. The fluid is made of nucleons (protons and neutrons), which are held together by the strong nuclear force. This is a crude model that doesn't explain all the properties of the nucleus, but it explains the spherical shape of most nuclei in their ground state. It also helps to predict the nuclear binding energy and to establish the energy balance for the reactions (Q-values). The binding energy E_B can be written in terms of (Z, N) as:

$$E_B = a_V A - a_S A^{2/3} - a_C \frac{Z^2}{A^{1/3}} - a_A \frac{(A-2Z)^2}{A} - \delta(A,Z) \tag{1.5}$$

where $A = N + Z$ is the number of nucleons and a_V , a_S, a_C and a_A are parameters. The five terms from the left to right of the formula correspond to a *volume energy term*, a *surface energy term*, the electrostatic mutual repulsion of the protons (*Coulomb energy term*), *asymmetry energy term* and a *pairing term* ($\delta(A,Z) = (N-Z)/(N+Z)$), respectively. If we consider the sum of the following five types of energies, then the picture of a nucleus as a drop of incompressible liquid roughly accounts for the observed variation of the binding energy of the nucleus.

The Weizsacker formula is a good starting point for defining a nuclear EoS, nevertheless it is based on the assumption that the system is at zero temperature and at saturation density $\rho_0 = 0.16\, fm^{-3}$. It is therefore necessary to define the nuclear interaction as a function of the neutron and proton densities (ρ_n, ρ_p) in order to obtain a more realistic and applicable EoS in the models.

1.2.2 Asymmetric nuclear matter

The binding energy in the case of asymmetric nuclear matter, can be generally expressed as a power series in the isospin asymmetry ($\delta = \rho_n - \rho_p$). To the 2nd-order in δ can be expressed as:

$$E(\rho,\delta) = E(\rho,\delta = 0) + E_{sym}(\rho)\delta^2 + O(\delta^4) \tag{1.6}$$

where $\rho = \rho_n + \rho_p$ is the nucleonic density, $E(\rho,\delta = 0)$ is the binding energy per nucleon of symmetric nuclear matter, and

$$E_{sym}(\rho) = \frac{1}{2} \cdot \frac{\partial^2 E(\rho,\delta)}{\partial \delta^2}\bigg|_{\delta=0} \tag{1.7}$$

is the nuclear symmetry energy [12]. The absence of odd-order term in eq.(1.7) is due to neutron-proton exchange symmetry in nuclear matter when the Coulomb interaction is neglected and the charge symmetry of nuclear force is assumed.

To go further and study the effect of the variation in δ, E_{sym} can be expanded around ρ_0 as

$$E_{sym}(\rho) = S_0 + \frac{L}{3}\left(\frac{\rho-\rho_0}{\rho_0}\right) + \frac{K_{sym}}{18}\left(\frac{\rho-\rho_0}{\rho_0}\right)^2 + O\left\{\left(\frac{\rho-\rho_0}{\rho_0}\right)\right\}^3 \tag{1.8}$$

where $S_0 = a_v^{sym}$ is the asymmetry energy at the saturation density similar with the term of the Bethe-Weizsacher formula, eq.(1.5), and

$$L = 3\rho_0 \frac{\partial E_{sym}(\rho)}{\partial \rho}\bigg|_{\rho=\rho_0} \tag{1.9}$$

$$K_{sym} = 9\rho_0^2 \frac{\partial^2 E_{sym}(\rho)}{\partial^2 \rho}\bigg|_{\rho=\rho_0} \tag{1.10}$$

are respectively the *slope parameter* and the *incompressibility parameter* of the asymmetry energy. They characterize the density dependence of asymmetry energy around saturation density and provide important information on behavior of E_{sym} at low and high densities. They can be estimated by adjustment between the experimental data and the theoretical models. Unfortunately most of the data came from the study of stable nuclei, the constraints are not restrictive enough. We can cite as an example the wide range of values of the L parameter between $20 - 120\,MeV$ [13].

Another way to parametrize E_{sym} is also often used:

$$\frac{E_{sym}}{A} = \frac{C_{kin}}{2}\left(\frac{\rho}{\rho_0}\right)^{2/3} + \frac{C_{pot}}{2}\left(\frac{\rho}{\rho_0}\right)^{\gamma} \tag{1.11}$$

where the first component is a kinetic term expressed according to the kinetic energy of a Fermi gas such as:

$$C_{kin} = \frac{1}{6m_{nuc}} \left(\frac{3\pi^2}{2} \right)^{2/3} \tag{1.12}$$

with $m_{nuc} \simeq m_n \simeq m_p \simeq 939\, MeV/c$, the nucleon mass. The second component is a potential energy term describing the nucleon-nucleon interaction. The density dependence comes exclusively from the parameter γ of the effective potential of nuclear interaction. The notion of "stiffness" of the potential, illustrated in fig.(1.6), appears here: E_{sym} is called **Asy-soft** for $\gamma < 1$ (potential term presenting a maximum between ρ_0 and $2\rho_0$) and **Asy-stiff** for $\gamma \geq 1$ (potential term continuously increasing with ρ) [15]. Indeed

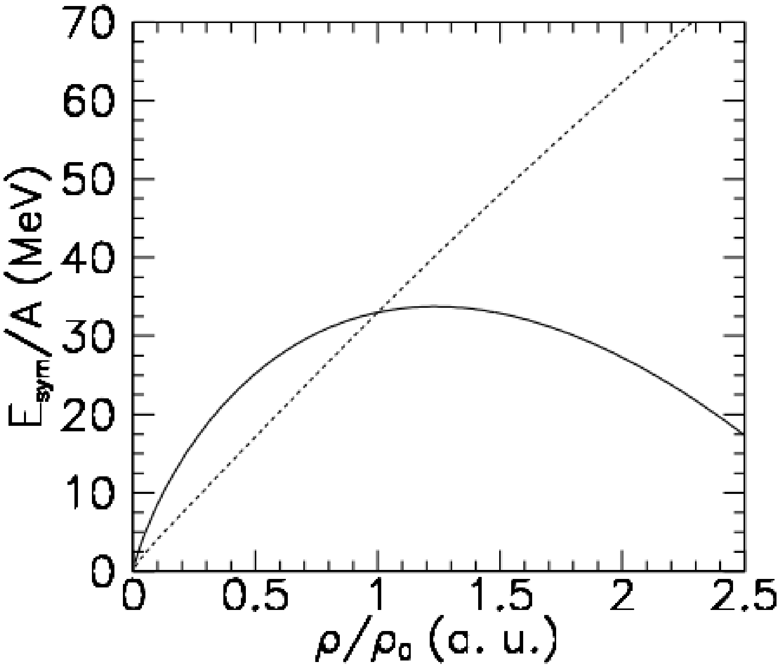

Figure 1.6: Density dependence of the symmetry energies used in the simulations presented here: Asy-soft (solid) and Asy-stiff (dashed) [14].

around ρ_0 the average field shows a strong variation according to the density in the case Asy-stiff and conversely in the Asy-soft case. From the above considerations, an experimental way to study the asymmetry energy term is to subject nuclear matter to large variations in isospin, for example using heavy ion collisions with stable and radioactive beams. As explained in the previous section according to the energies, the species involved, as well as the violence of the collisions, the mechanisms involved differ greatly. The difficulty is then to define the density regions explored experimentally, the models applicable to the study of asymmetry energy, but also the observable influenced by the variation of this latter.

1.3 Observables sensitive to asymmetry energy

Sources of information on $E_{sym}(\rho)$ are essentially limited to experimental and astrophysical observations. However, a comparison between measurements and predictions from theoretical models has allowed the scientific community to constrain asymmetry energy around saturation density. Experimentally, asymmetry energy affects the isotopic distributions of products from heavy ion collisions involving partners with a large difference in isospin. In the context of this thesis, we are interested in observables that can be measured in heavy ion collisions at intermediate energies, such as **isoscaling**, **isospin transport** and in particular, in the study of the isotopic distribution forms, that will be described in this section.

1.3.1 Isoscaling

In the study of the isoscaling we use the Grand canonical ensemble hypothesis. In this approach, the production rate of the isotopes is governed by the chemical potentials of the two nucleons, μ_p and μ_n, the temperature T and the individual binding energies of the different isotopes $B(N, Z)$:

$$Y(N,Z) = F(N,Z,T)\exp\left(\frac{B(N,Z)}{T}\right)\exp\left(\frac{N\mu_n + Z\mu_p}{T}\right) \tag{1.13}$$

where the chemical potentials are related to the density. The term $F(N,Z,T)$ includes information about the change in production rate from secondary disintegration and the temperature of the isotope considered.

Isoscaling is an empirical scaling law observed experimentally on a variety of reactions covering a wide range of energy [16, 23]. This law relates the production rates of the same isotope and the ratio between the production rates of a given fragment (N,Z) measured in two reactions, 1 and 2, different by their total N/Z values of the system, satisfying a scaling behavior:

$$R_{21}(N,Z) = \frac{Y_2(N,Z)}{Y_1(N,Z)} = C\exp(\alpha N + \beta Z) \tag{1.14}$$

where $\alpha = \Delta\mu_n/T$ and $\beta = \Delta\mu_p/T$ reflect the differences between the chemical potentials of neutrons and protons in both reactions and C is a normalization constant.

The dependencies in N and Z become more visible if, for each value of Z, R_{21} is drawn as a function of N for all the isotopes in a semi-logarithmic graph. The resulting slopes give us the values of α for each value of Z.

The accuracy of the isoscaling described by eq.(1.14) can be compactly displayed if one plots the scaled isotopic ratio,

$$S(N) = R_{21}(N,Z)\exp(-\beta Z) \tag{1.15}$$

as a function of N. For all elements, $S(N)$ must lie along a straight line on a semilog plot when eq.(1.14) accurately describes the experimental data, see fig.(1.7). When we consider a system in equilibrium, at the temperature T and pressure (P), the number (or yield) of a nucleus composed of N neutrons and Z protons is given by

$$Y_i(N,Z) \propto \exp\left\{-\frac{1}{T_i}\left[G_{\text{nuc}}(N,Z) - \mu_{ni}N - \mu_{pi}Z\right]\right\} \tag{1.16}$$

where the index i specifies the reaction system, with the total neutron and proton numbers N_i^{tot} and Z_i^{tot} and G_{nuc} stands for the internal Gibbs free energy of the (N,Z) nucleus. The net Gibbs free energy G_{tot} for the system is related to the chemical potentials $\mu_{i,n}$ and $\mu_{i,p}$ by $G_{\text{tot}} = \mu_{nr}N_i^{\text{tot}} + \mu_{pi}Z_i^{\text{tot}}$. According to eq.(1.14) and the consequence of

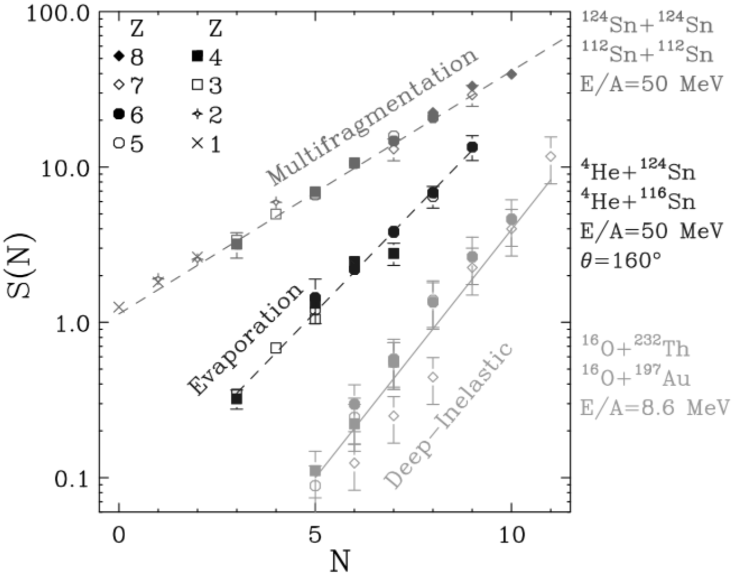

Figure 1.7: The scaled isotopic ratio $S(N)$ is plotted as a function of the neutron number N, using the best fit value of b obtained from fitting isotopes with $Z \geq 3$. The data points marked as *"multifragmentation"* show values of $S(N)$ extracted from isotope yields with $1 \leq Z \leq 8$ measured for multifragmentation events in central $^{124}Sn+^{124}Sn$ and $^{112}Sn+^{112}Sn$ collisions at $E/A = 50\,MeV$, with $\alpha = 0.37$, $\beta = -0.40$. The scaling behaviour for evaporation process is illustrated by the reactions ^{4}He+^{116}Sn and ^{4}He+^{124} Sn plotted next to the label "evaporation" with $\alpha = 0.60$, $\beta = -0.82$. Systematics of the strongly damped binary collisions is represented by the data of ^{16}O induced reactions on two targets ^{232}Th and ^{197}Au plotted next to the label "deeply inelastic" with a $\alpha = 0.74$, $\beta = 21.1$. [17]

establishing the chemical and thermal equilibrium is that the isoscaling law is verified if:

$$\alpha = \frac{\mu_{n,2} - \mu_{n,1}}{T}$$
$$\beta = \frac{\mu_{p,2} - \mu_{p,1}}{T} \tag{1.17}$$

For each given Z, the dependence of G_{nuc} on N, assuming gradual changes, takes the form

$$G_{\text{nuc}}(N, Z) = a(Z)N + b(Z) + C(Z)(N - Z)^2/A \tag{1.18}$$

Because the important range of N is limited for a given Z, this expansion is practically sufficient even when G_{nuc} contains surface terms, Coulomb terms and that term $C(Z)$ can be seen as the asymmetry energy term, i.e.,

$$C(Z) = \frac{E_{sym}}{A} = C_{sym}\,.$$

This fact can be proved by a straightforward analytical calculation, if a typical liquid-drop mass formula is assumed as an example.

The most probable value of the number of neutrons $\langle N_i(Z)\rangle$ associated with each Z corresponds to the maximum of the isotopic distribution in relation to the number of neutrons, so:

$$\frac{\partial}{\partial N}\{-G_{nuc}(N,Z) + \mu_{n,i}N + \mu_{p,i}Z\}\bigg|_{N=\langle N_i(Z)\rangle} = 0 \tag{1.19}$$

A straightforward calculation, using the specific form of G_{nuc} of eq.(1.18) results in,

$$C_{sym}\left[1 - 4\left(\frac{Z}{Z + \langle N_i(Z)\rangle}\right)^2\right] = \mu_{n,i} - a(Z) \tag{1.20}$$

Thus from eq.(1.20), subtracting a system (2) from a system (1), we obtain:

$$\frac{\alpha}{\left(\frac{Z}{\langle A_1(Z)\rangle}\right)^2 - \left(\frac{Z}{\langle A_2(Z)\rangle}\right)^2} = 4\frac{C_{sym}}{T} \tag{1.21}$$

with $\langle A_i(Z)\rangle = Z + \langle N_i(Z)\rangle$, relating the isoscaling parameter α, the $(Z/A)^2$ of fragments, and the symmetry energy coefficient C_{sym} which is a function of (T, P). Interestingly, this relation does not involve the terms in G_{nuc} other than the symmetry-energy term [18].

1.3.2 Form of isotopic distributions

In eq.(1.16), we wrote the Yield of a nucleus composed of N neutrons and Z protons as a function of the free energy $G(N,Z)$, it is possible to re-write it as:

$$Y_i(N,Z) = \exp\left[-K(N,Z) + \alpha_i N + \beta_i Z + \gamma_i\right] \tag{1.22}$$

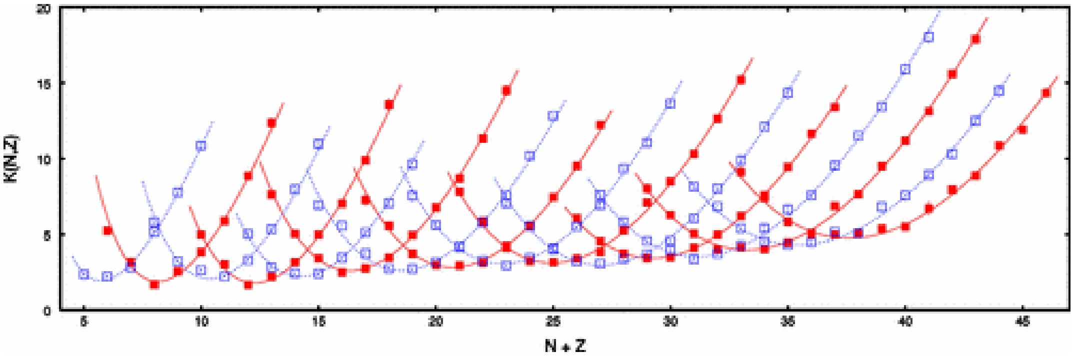

Figure 1.8: The values of $K(N,Z)$ for $3 \leq Z \leq 18$ are shown by symbols for the abscissa of $N + Z$. The values are obtained by combining the results of ^{40}Ca $+^{40}$ Ca,^{48} Ca $+^{48}$ Ca,^{60} Ca $+^{60}$ Ca and ^{46}Fe $+^{46}$ Fe simulations. The error bars show the statistical uncertainty due to the finite number of events. The curve for each Z was obtained by fitting $K(N,Z)$ using eq.(1.24).

where α_i and β_i are the parameters of the isoscaling. The factor γ_i is a constant that depends on the reaction i whereas $K(N,Z)$ is a function that is independent of the system. By combining the Yields of several systems [24], an overall distribution $K(N,Z)$ can be constructed:

$$K(N,Z) = \sum_i w_i(N,Z)\left[-\ln\left(Y_i(N,Z)\right) + \alpha_i(Z)N + \gamma_i(Z)\right] \tag{1.23}$$

where i represents each reaction. The average weights $w_i(N,Z)$ are determined by minimizing the statistical errors of $K(N,Z)$ for a given isotope. The isoscaling parameters $\alpha_i(Z)$ are the parameters defined in the previous section.

Fig.(1.8) shows the distribution of the function $K(N,Z)$ as a function of A for all isotopes $Z = 3-18$, obtained from AMD simulations of ^{40}Ca+^{40}Ca,^{48} Ca+^{48}Ca,^{60} Ca+^{60}Ca and ^{46}Fe $+^{46}$ Fe. These reactions have been chosen to cover a wide range of isotopes produced. The distributions $K(N,Z)$ for each value of Z can be adjusted with a quadratic function:

$$K_i(N,Z) = \xi(Z)N + \eta(Z) + \zeta(Z)\frac{(N-Z)^2}{N+Z} \tag{1.24}$$

where $\xi(Z), \eta(Z), \zeta(Z)$ are the fitting parameters. The parameter $\zeta(Z)$ of the quadratic term in $(N-Z)$ is associated with the symmetry energy C_{sym} at a finite temperature and a subsaturation density. If the fragments are in chemical and thermal equilibrium, $\zeta(Z)$ can be connected to the symmetry energy $\zeta(Z) = (c_V + c_S A^{-1/3})/T$ where the coefficients of volume and surface of the symmetry energy satisfy $c_V \sim -c_S$ for the nucleus in its ground state. Indeed, advanced mass laws introduced the dependence of A of $c(A)$ as a surface effect. The extraction of the symmetry energy of the binding energies is not obvious, even for the fundamental states. For example, we can use the difference in energy of neighboring nuclei to extract the symmetry energy term. The resulting value shows a large fluctuation in the nuclear chart due to the effects of pairs, but the assumption of $c(A) = c_V + c_S A^{-1/3}$, with the standard terms of volume, area, Coulomb and pairing, results in a reasonable value of the coefficients. If the binding energies calculated with AMD are adjusted, we obtain $c_V = 30.9\,MeV$ and $c_S = -35.2\,MeV$ [24].

1.3.3 Isospin transport

In nuclear collisions the two nuclei in contact can exchange nucleons, this phenomenon is called *isospin transport*. It depends essentially on the initial composition of the two partners, their contact time and the asymmetry energy term of the nuclear state equation.

The isospin transport is defined by the currents $\vec{j}_n$ and $\vec{j}_p$ of neutrons and protons between the two nuclei in contact during the collision, such as:

$$\vec{j}_{n,p} = D^{\rho}_{n,p}\vec{\nabla}\rho - D^{\delta}_{n,p}\vec{\nabla}\delta \tag{1.25}$$

where $\rho = \rho_n + \rho_p$ is the density of the medium, $\delta = (\rho_n - \rho_p)/\rho$ the isospin, $D^{\rho,\delta}_{n,p}$ are transport coefficients of neutrons and protons in density and isospin [19]. According to eq.(1.25) we have:

$$\vec{j}_n - \vec{j}_p = (D^{\rho}_n - D^{\rho}_p)\vec{\nabla}\rho - (D^{\delta}_n - D^{\delta}_p)\vec{\nabla}\delta \tag{1.26}$$

The first term of eq.(1.26), called the drift (or migration) term of isospin (*isospin drift*), is associated with the density gradient. It is connected to the derivative (slope) of asymmetric energy, such as:

$$D^{\rho}_n - D^{\rho}_p \propto 4\delta \cdot \frac{\partial E_{sym}}{\partial \rho} \tag{1.27}$$

The second term of eq.(1.26), called diffusion term of isospin (*isospin diffusion*), is associated with the isospin gradient of the system. It is connected to the absolute value the energy of asymmetry, such as:

$$D_n^{\delta} - D_p^{\delta} \propto 4\rho \cdot E_{sym} \tag{1.28}$$

In summary, during a heavy ion collision, a process of equilibration of the neutron-proton ratio (N/Z) takes place and is governed by the competition between:

- the isospin drift, which is responsible for the transport of neutrons to low density regions. According to eq.(1.27) this term depends on the slope of the asymmetry energy.
- isospin diffusion which minimizes the N/Z gradient and is responsible for transporting neutrons from a high N/Z region to a low N/Z region. According to eq.(1.28) this term depends on the absolute value of the asymmetry energy.

It is therefore interesting to explore experimentally collisions of different N/Z ratios between the projectile and the target, and to study in particular the asymmetry of the different products formed in the peripheral reactions. Indeed in such collisions a low density is expected in the region of mid-rapidity creating a density gradient. Because of this density gradient, we can expect a neutron flux towards the mid-rapidity zone, which is higher in the case of asymmetric asystiff energy than asysoft, for more detail see ([20], chap.5).

Chapter 2

FAZIA Project

The project started in 2001. At the beginning, it was a french-italian initiative named *AZ4Pi* (in the framework of an Integrated Program for Scientific Cooperation). AZ4Pi was created to improve the detection and identification, in charge and mass (Z,A), of charged particles released in heavy-ion induced reactions around and below the Fermi energy, within the scope of the EURISOL project.

In April 2006, the FAZIA (*Four π AZ Identification Array*) project has been launched in order to progress in the design of a new multidetector. The collaboration has expanded and groups together more than 10 institutions in Nuclear Physics from 6 different countries (France, Italy, Poland, Spain, Romania, India) [25].

The main requirement of FAZIA is the modularity and portability: in fact, it was designed to measure in various laboratories, in several setup and coupled to different detectors. Another important objective is to maximize unit identification for charges and masses of detected nuclei. For doing this, there was a phase of *Research and Development* (2006-2014), described in [26]. In the present situation it clearly discriminate charges up to $Z \sim 55$ and masses up to $Z \sim 25$. The great complexity and the fine granularity of the apparatus implies a difficult scalability and thus a relatively poor angular coverage: in fact, a 16-telescope is the smallest indipendent FAZIA unit, which covers only around 0.05% of the full solid angle at 1 m distance from the target [27].

In this chapter we will describe, in the first part, the detectors and the coupling INDRA-

FAZIA made in the firsts month of 2019 in GANIL (*Grand Accélérateur National d'Ions Lourds*), then the identification techniques.

2.1 Overview of FAZIA

In order to meet the initial specifications concerning the portability of FAZIA, the latter was conceived as an assembly of unit blocks. A block corresponds to a compact assembly of 16 telescopes, each composed of three detection stages: *Si1- Si2- CsI(Tl)*. These three detection stages have thicknesses of $300\,\mu m$, $500\,\mu m$ and $10\,cm$ respectively. They have a transverse area of $2x2\,cm^2$. Fig.(2.1) shows a block of FAZIA in its final configuration (exploded view). The 16-telescopes *Si1-Si2-CsI(Tl)* are represented on the left, followed by the fixation system. In the middle of the figure are visible the eight front-end electronic cards (*FEE card*) allowing the control and the read-out of the telescopes, followed by the three control boards of the block (for further details on the electronics, see [27]). The entire electronics of a FAZIA block is fixed on a copper plate with some

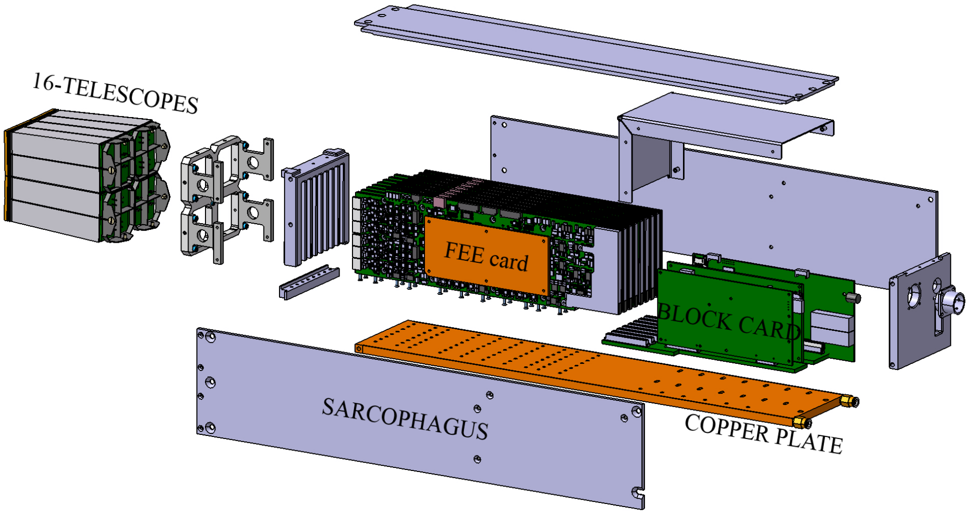

Figure 2.1: Exploded view of a block of FAZIA. The size of a block is $70x10x10\,cm^3$ and its weight is about $15\,kg$.

channels, in which circulates a heat-carrier fluid, that makes possible to dissipate the heat generated by the electronic components during the operation under vacuum. The set is integrated in a sarcophagus to protect the electronics from external shocks, to shield one block to another, improve the electromagnetic compatibility between the different blocks and finally facilitate its movements. The supply of a block is operated by a cable of 48 $V\,DC$ and the communication is carried out via two optical fibers. These three connections are at the back of the block. Finally, the cooling system is directly connected to the copper plate of the block using two pipes, connected to an external cooler operating with a mixture of distilled water and glycol (30%).

2.1.1 Detectors

We will briefly describe the two different detectors composing the FAZIA telescope: **Silicon detector** and **Scintillator**.

Silicon detector (*Si1 and Si2*) Among the detectors used in Nuclear Physics to detect charged particle, the p-n junction semiconductor detector, in the follow *silicon detector*, is one of the best choice. They allow to determine the incident ion energy better than other detectors because the response is linear in energy and inside them the production, at the same energy, of *charge carriers* is higher. Indeed, to create an *electron-hole pair* it requires only $\sim 3\,eV$ (on average) instead of, for example, $\sim 35\,eV$ (on average) to create an *electron-ion pair* in the gas detectors.

The electrical potential generated by the excess of holes (h) in the p-zone and the surplus of electrons (e^-) in the n-zone creates a zone of depletion between the two junctions. Applying an external voltage with the cathode to the p-zone and the anode to the n-zone, the ($e^- - h$) are pulled out the depletion zone, that became larger. In this way, the only free particles that are located inside the junction are those that are generated by the passage of a particle inside the detector, which loses energy in the depletion region and excites the electrons that make the jump from the valence band to the conduction band, forming *electron-hole pairs*. Due to the electric field, they move inside the silicon and are collected by the electronics welded to the detector. Since the signals coming from the detector are generally very weak, they are pre-amplified, amplified and then recorded [28].

What we have described until this point in the paragraph are the general features and the physics behind the functioning of the silicon detector and have general validity. Now, we will briefly summarize the main achievements of the *phase R&D*, that optimized the performance of the silicon detector, introducing the use of:

- *tilted silicon*, in order to reduce the *channeling* phenomena and the consequently *straggling* effects that are responsible for the reduction of the energetic resolution;
- the *neutron transmutation doped* (n-TD) to optimize the dopant homogeneity, in order to increase the identification capacity;
- the *reverse mounted* of the silicon (i.e. the charged fragments impinge on the low field side of the detector), in this way, on average, the collection time is greater and allow to obtain a better mass identification.

Scintillator (*CsI(Tl)*) The third layer of the telescope is a CsI(Tl) detector of $10\,cm$ in the shape of a square pyramid trunk. As radiation passes through the scintillator, it excites the atoms and molecules making up the scintillator causing light to be emitted. Then this light is collected by a semiconductor device that converts light into an electrical current: a squared photodiode ($21x21\,mm^2$) placed at the end of the telescope. The Cesium Iodide is an alkali halide crystal and is an inorganic scintillator that is generally doped with Sodium or Thallium. This is essential to increase the scintillation efficiency, reduce self-absorption and have the light output in the desired wavelength.

The CsI(Tl) is composed with a relatively high atomic number $Z = 53$, which gives it, thanks also to the high density ($4.5\,gr \cdot cm^{-3}$), a considerable stopping power capacity for light charged particles.

The role of the CsI(Tl) is manifold:

- to stop particles that have high energy, making possible the measure of energy and also the identification using the $\Delta E - E$ (Si2-CsI) matrix, see sec.(2.4);
- identify in charge and mass light charged particles ($Z = 1 - 3$) using the *Pulse Shape Analysis* (PSA), see sec.(2.4);
- be used as a veto to "clean-up" the $\Delta E - E$ (Si1-Si2) matrix from the *punch through*[1] events.

2.2 Overview of INDRA

The INDRA multi-detector has already been the subject of several theses and publications [29, 30]; so we will describe in this section only the essential information of this detector. INDRA (*Identification de Noyaux et Détection avec Résolutions Accrues*) is a highly segmented detector constructed for the detection of multiple light charged particles ($Z \leq 2$) and fragments ($Z > 2$) emitted in heavy ion collisions. Its design responds to experimental constraints specific to heavy ion collisions at the energies and beams available at GANIL in the early nineties: from Carbon to Uranium, with so-called intermediate energies varying in the range $10 < E < 100\,MeV/u$, the upper limit depending on the mass of the projectile.

The main characteristics of INDRA are:

- The capability to identify in charge a large number and a large variety of charged particles and fragments (charge resolution from proton to Uranium and mass resolution up to $Z = 4 - 5$).
- A large coverage of the solid angle around the target (90%).
- High granularity (336 identification modules).
- Very low energy thresholds while keeping a wide range of identification in energy and momentum (from 1 MeV to 4 GeV).

---

[1] Punch through events are those particles that have enough energy to go outside the detector.

2.2.1 Geometry

The optimal configuration of a multi-detector is a compromise between its size and its number of elements. Indeed, a large number of components makes it possible to limit the multiple counting rate but also has the effect of increasing the number of dead zons as well as the probability of diffusing particles from a component towards a neighbor component. Fig.(2.2), shows a schematic section of the multidetector. INDRA's granularity, i.e. 336 independent identification modules, was optimized to detect a maximum of 40 light charged particles in coincidence with 10 fragments, while having a multiple count rate lower than 5%.
INDRA is originally made up of 17 rings with cylindrical symmetries assembled around the axis of the beam. The target holder is located between the rings 12 and 13 ($\theta \in [88^o; 92^o]$), with a solid angle loss of approximately 3.5%, while two openings at the front and behind, let the beam pass (respectively $\theta \in [176^o; 180^o]$ and $\theta \in [0^o; 2^o]$), for a solid angle loss of about 0.2%.

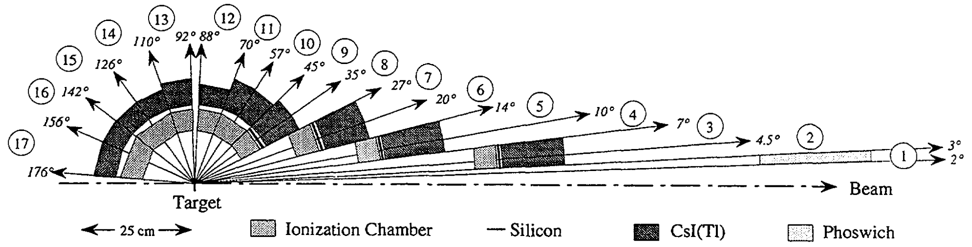

Figure 2.2: Geometrical outline of the INDRA detector (cut along the beam axis). The detectors are arranged in 17 rings that are coaxial with the beam axis.

2.3 Coupling INDRA-FAZIA

As we have seen previously, the development of the FAZIA multi-detector has been initiated to allow the identification in (Z, A) of the reaction products, which was not possible with INDRA. However, the demonstrator version of FAZIA (12 blocks) does not have sufficient angular coverage to allow more exclusive selections, using some global variable, such as tranverse energy or light particle multiplicity, as selector for the impact parameter. This is why the "back" part of INDRA is kept, FAZIA replacing only the front part. The reactions of the experiment (e709) are $^{58,64}Ni +^{58,64} Ni$ in the energetic range $(35 - 50\, MeV/u)$.
We will present briefly the mechanical coupling between INDRA and FAZIA, before presenting the coupling of the acquisition systems.

2.3.1 Mechanical coupling

The FAZIA demonstrator used in the case of the coupling corresponds to a *wall* configuration of 12 blocks. These cover the polar angles from $1,5^o$ to 14^o and the structure supporting them (organized in four triplets) is placed at a distance of 1 m from the target. The INDRA rings 6 to 17 complete the detection device (from 14^o to 176^o), thus covering up to 80% of the solid angle. Note also that in the case of this coupling, the INDRA telescopes rings covering the polar angles of 14^o to 45^o will be equipped with silicon detectors with a thickness of $150\,\mu m$. This replacement make it possible to push the gains of the pre-amplifiers of these silicon detectors to the maximum (the signals will be smaller) and to improve the resolution, allowing an isotopic identification up to Z = 8 in INDRA.
Fig.(2.3) shows the experimental device that was installed in the INDRA reaction chamber, on the experimental area D5 at GANIL.

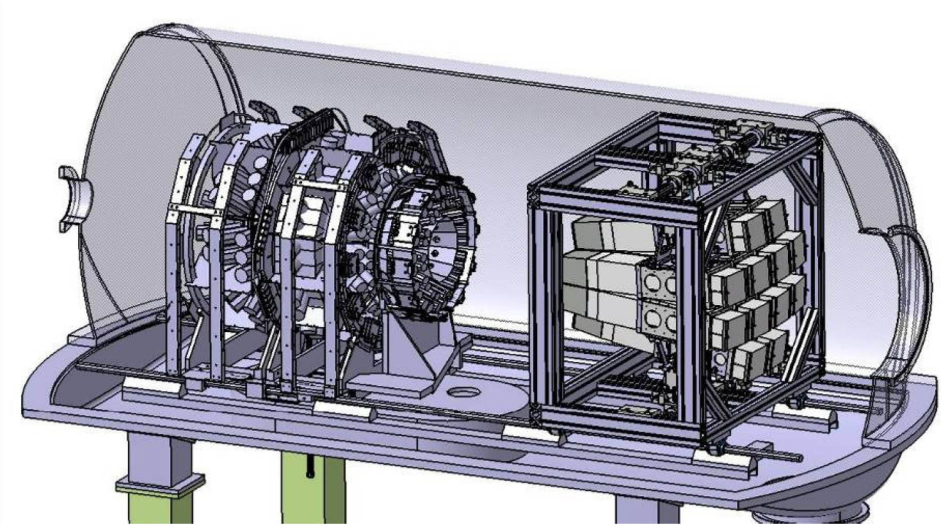

Figure 2.3: Coupling INDRA-FAZIA, placed on the left INDRA and on the right FAZIA.

2.3.2 Acquisition coupling

The coupling of these two multi-detectors requires also to couple their data acquisitions. To do this, the *VXI CENTRUM module* developed at GANIL is used to correlate the events detected in each of the two multi-detectors. Each of the two acquisitions is connected to this module then serving as a common clock (operation in time marker mode: timestamp).

Fig.(2.4) shows the data acquisition timeline in the semi-autonomous coupling configuration of INDRA and FAZIA. The INDRA purple arrow corresponds to the first particle detected in INDRA, then opening the coincidence window (FC) with a width of $240\,ns$ at the time $t_0 = 0\,ns$. It is also at this time that the dead time (TM) of the INDRA acquisition begins, during which time it can not be processed another event. In the case that the detected event respects the conditions of the triggering system, the validation signal VALID1 is emitted by the acquisition at the time $t_1 = 250\,ns$. It is this signal that is used to query the time marker with the CENTRUM for the INDRA event. The slow acceptance signal (AVL) starts at time $t_2 = 280\,ns$ and has a width of 960 ns. The latter was set at this value because it corresponds to the width of the distribution of the time difference between INDRA and FAZIA time markers during the coupling test phases performed at GANIL during the months of June and July 2018.

If a FAZIA local trigger signal (symbolized by the FAZIA purple arrow) is received while this window is open, the acquisition requests the CENTRUM time marker for the FAZIA event. The VETO FAZIA blocking signal, starting at time $t_3 = 1240\, ns$, makes it possible to prevent the FAZIA acquisition from sending requests to the CENTRUM in order to avoid the latter from triggering on a new reaction while INDRA is busy processing the previous. This blocking signal is stopped when the INDRA acquisition has finished processing the event and is ready to accept another at time t_f.

In the event that no trigger from FAZIA is received during the opening of the (AVL) window, the acquisition of INDRA resets and is ready to process a new event. In the case that an event of INDRA and FAZIA are considered as coming from the same reaction, these are sent in the NARVAL acquisition system of GANIL. A merger module

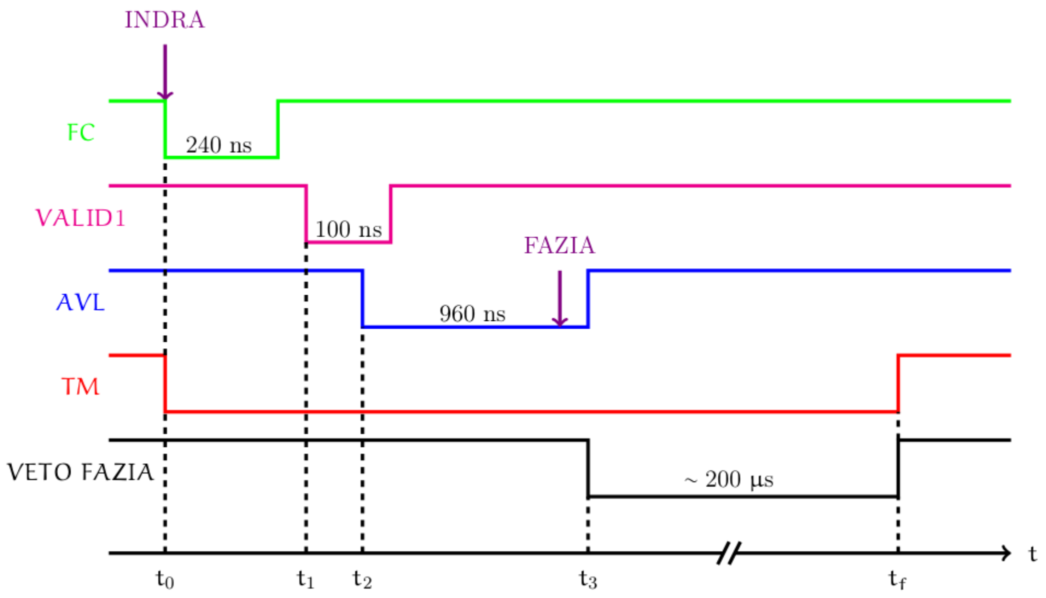

Figure 2.4: Chronogram of the semi-autonomous mode of operation of the coupling of the acquisitions INDRA and FAZIA.

then allows merging the two events into one with two substructures: one for the particles detected in INDRA and the other for those detected in FAZIA. Once built, the entire event is stored on a hard disk [31]. To better understand how the acquisition works, we will describe the FAZIA local trigger [27].

FAZIA local trigger On both FPGAs of the FEE cards, fast trapezoidal shaping filters are implemented on the $QH1$, $Q2$, $Q3$ signal (produced, respectively in the Si1, Si2 and CsI detectors) in order to generate local trigger. For each front-end the user can choose the trigger timeout, the trigger source (logic OR among any combination of Si1, Si2 and CsI) and the kind of threshold: i.e. one may use the low threshold only (trigger is produced when the maximum amplitude of shaped signal is larger than it) or both low and high threshold (trigger is produced when the maximum amplitude of shaped signal is between them).

The FAZIA trigger system is multiplicty based: on each block the Block Card (BK) counts the local trigger and sends the total to the Regional Board (RB) every $40\,ns$ through the optical link. The RB collects all the multiplicity values coming from each block and applies up to eight programmable rules. For each one the user can choose the block checked by the rule, the multiplicity threshold and the downscale factor (K). The RB will then integrate inside a time window the multiplicities coming only from the blocks specified by the rule, and it will produce a "rule trigger" only if the integrated value overcomes the multiplicity threshold. The trigger is the accepted once every K occurences.

2.4 Particle identification methods

Different identification methods can be used to identify the fragments stopped in different layers of FAZIA, that are also the same methods used for INDRA. These methods are implement inside an important toolkit for the analysis and simulation, a C++ library called *KaliVeda* [32] and based on the *ROOT* [33] analysis framework. Kaliveda was originally developed in GANIL to provide simulation and analysis tools for the INDRA detector array.

It has then evolved, thanks to the addition of many other general tools of interest, such as:

- energy loss, stopping power and range calculations for ions with energy $E = 1 - 100\, MeV/u$;
- particle reconstruction from energy losses in arbitrary multidetector geometries;
- particle identification algorithms exploiting PSA and $\Delta E - E$ matrices;
- multi-particle physics analysis;
- inteface to the GEMINI++ statistical decay code.

This tools were extensively used in the next chapters to analyze the data.

During my internship (15/10-30/11/2018) at LPC (*Laboratoire de physique corpusculaire in Caen*), I was in charge to identify particles for the data from the reaction $^{48}Ca +^{40} Ca$ of the FAZIA-Sym experiment, perfomed at LNS (*Laboratori Nazionali del Sud*) prior to the INDRA-FAZIA coupling. All the matrices in the chapter are made using this data-set for one of the FAZIA telescope.

2.4.1 $\Delta E - E$ technique

One of the most common technique used for the particle identification is the $\Delta E - E$ correlation, exploiting the energies deposited in two detectors, placed in succession, in the hypothesis that the particle stops in the second. The operating principle is based on the mechanism of energy loss of an ionizing particle passing through a material. The loss of energy per unit of length (*stopping power*) is well described by the *Bethe-Block formula* ([34], pp.24-32).

We are in a non-relativistic regime, so the Bethe-Block formula can be approximated as:

$$\frac{dE}{dx} \simeq C\frac{Z^2}{v^2} \tag{2.1}$$

where dE is the energy lost in the infinitesimal thickness dx, Z and v are respectively the atomic number and the velocity of the particle and C is a constant that depends on the material. Furthermore, in this regime we have

$$E = \frac{1}{2}Mv^2 \tag{2.2}$$

where E is the cinetic energy of the particle and M its mass. If we put eq.(2.2) in eq.(2.1), we obtain:

$$E\frac{dE}{dx} = kMZ^2 \tag{2.3}$$

where $k = C/2$. If we produce a plot with the correlation between the energy lost inside the first detector (ΔE) and the energy released in the second one (E_{res}), we obtain that, varying the energy, the particles are placed along different curves for different values of the MZ^2 product [28].

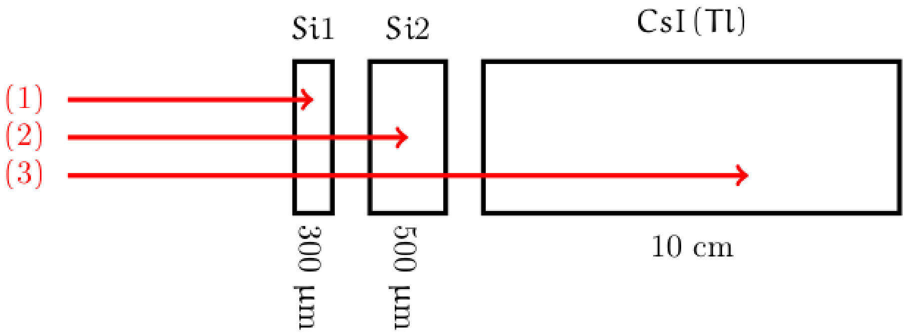

Figure 2.5: Schematic view of a *Si1-Si2-CsI(Tl)* FAZIA telescope. The three red arrows represent three incident particles, each stopping in a different detection stage.

In order to use this technique, we have to know where the particle stops. In fact, if we look at fig.(2.5) the correlation $\Delta E - E$ can be used only for particle (2) and (3) with two different matrices, respectively: $\Delta E - E$ $(Si1 - Si2)$ matrix, see fig.(2.6); $\Delta E - E$ $(Si2 - CsI(Tl))$ matrix, see fig.(2.7). In the second case, we should have used the correlation $((Si1 + Si2) - CsI(Tl))$, but the energy lost in the first layer is negligible with respect to the one in $Si2$ if the particle has enough energy to reach the last layer of the telescope. Moreover, if we look at fig.(2.7b) is shown the isotopic separation for the $\Delta E - E$ $(Si2 - CsI)$ matrix, that we obtain even if the CsI, as we will see later, doesn't have this resolution. This is due to the fact that for the $\Delta E - E$ technique is more important the resolution of the thin layer (ΔE).

2.4.2 Pulse Shape Analysis (PSA)

PSA exploits the different signals shape of the produced by fragments with different Z and A, due to the process of collection of the carriers inside the detector.

PSA in silicon detector A particle, passing through the sensitive volume of the silicon detector, generates a linear density of charge along its path. For nuclear fragments, this density can be so high that the so-called *ionization column* behaves like a plasma of electrons and holes. Only the electrons and the holes closest to the surface of the ionization column are affected by the electric field present in the region of space charge and migrate towards the electrodes: it is therefore necessary a finite time for the electric field to penetrate into the plasma region and make all the electrons and holes migrate to the electrodes. This time is called *plasma time*.

The time required for all the free charges produced by the incident ion to be collected by the electrodes defines the "rise time of the charge signal". It should also be noted that, since the ions stop completely inside the detector, the charge density profile follows the Bragg curve, i.e. there is maximum density of free charges at the end of the range. For this reason it is usual to have the ion engraved on the side opposite to the one where the junction develops, that is on the weak field side. In this configuration, a heavy ion, which therefore has a smaller range than a lighter ion, generates in its passage a region of high charge density precisely where the electric field has a lower intensity: this will lead to a long time to collect the charge with respect to a lighter ion (which has a greater range) and generates a plasma of electrons and holes of lower density in a region where

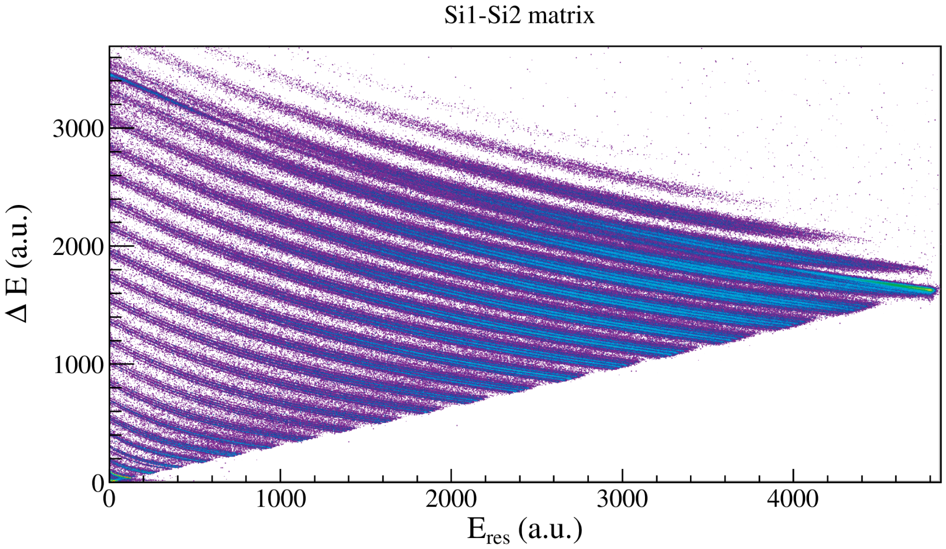

(a) The whole data collected.

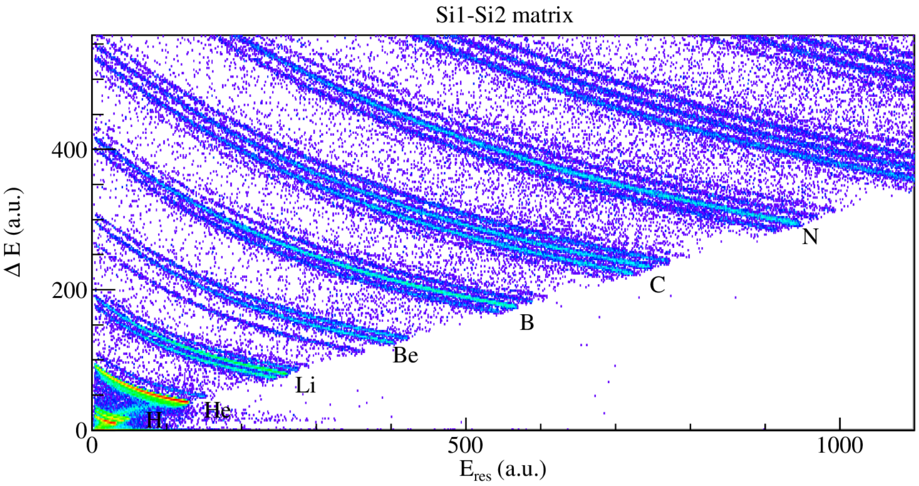

(b) Zoom to show the isotopic separation.

Figure 2.6: $\Delta E - E$ matrix correlation between the energies deposited in Si1 and Si2.

the electric field has greater intensity [26].

From fig.(2.5), we can use this method for the particle (1), using the correlation between the energy deposited in the silicon detector ($E(Si1)$) and the maximum ampli-

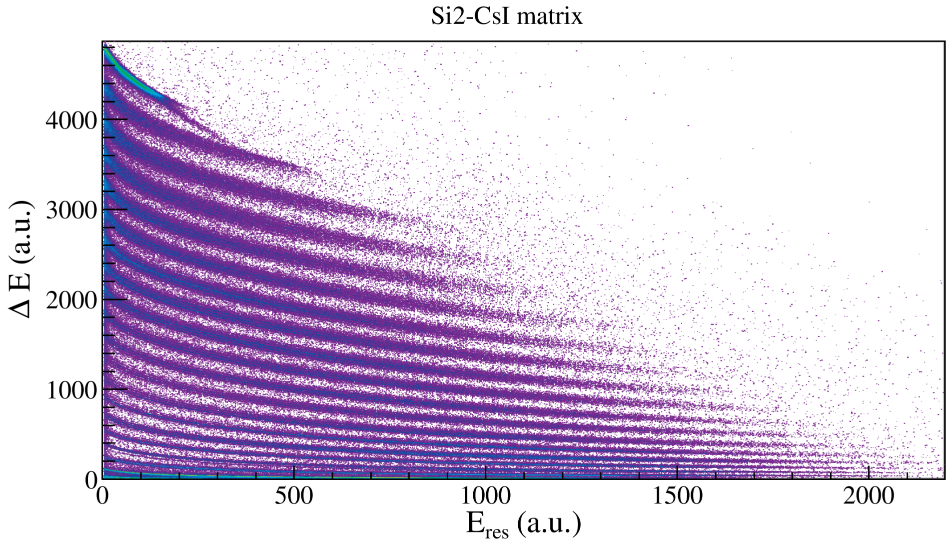

(a) The whole data collected.

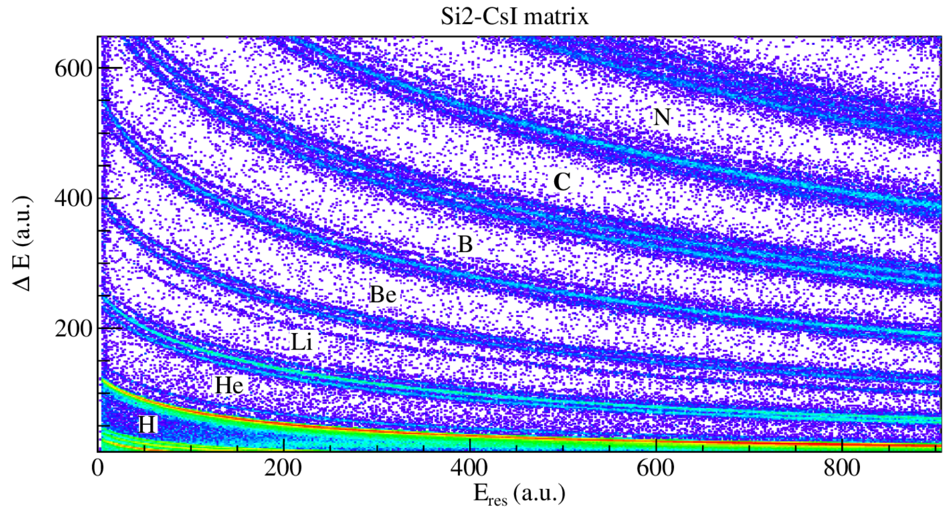

(b) Zoom to show the isotopic separation.

Figure 2.7: $\Delta E - E$ matrix correlation between the energies deposited in Si2 and CsI.

tude of the current signal collected (I_{max}), see fig.(2.8). Indeed, the FAZIA electronics is equipped with a custom developed pre-amplifier which gives also a current signal together with the charge, obtained through a differentiation of the charge signal.

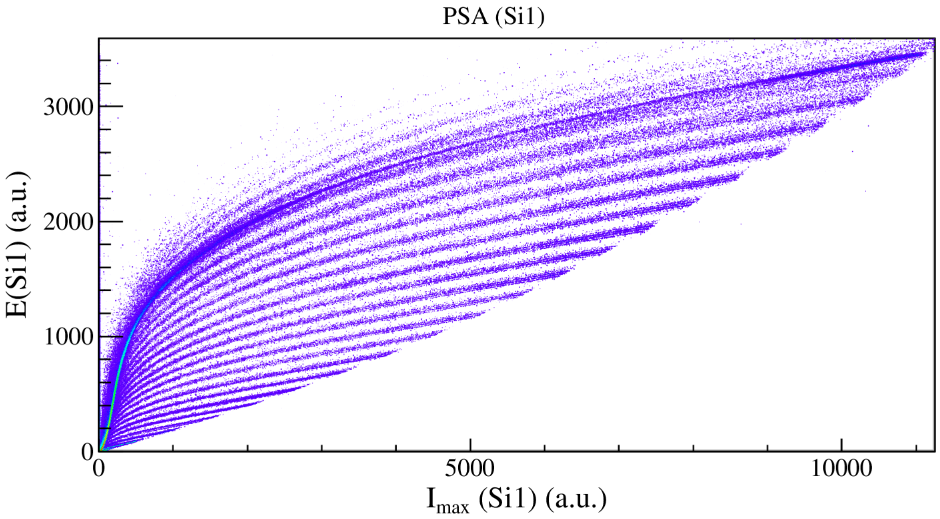

Figure 2.8: PSA in Si1, correlation between the energy deposited and the maximum amplitude of the current signal collected.

PSA in CsI In the case of CsI (Tl) detectors the identification of light particles is made possible by the fact that the temporal trend of the scintillation light depends on energy, as well as from Z and A [34].

In fact, the intensity of the light emitted ($I(t)$) from the sites activated by the energy deposited by the ion, can be described as the sum of two-components with an exponential behaviour depending on time: one *slow component*, with time constant (τ_s) and one *fast component* (τ_f). If we have the same amount of emitted light what we observe is that the intensity of the fast component depends on (Z,A) of the ion while the slow component remain indipendent. The scintillation light intensity can be written as:

$$I(t) = A \exp\left(\frac{-t}{\tau_{\mathrm{f}}}\right) + B \exp\left(\frac{-t}{\tau_{\mathrm{s}}}\right) \tag{2.4}$$

where A, B are constants depending on the total light intensity emitted by the two components. Fig.(2.9), represent the scintillation light intensity as a function of the time.

It is possible to resolve the fast and slow information by treating the detector signal with two shapers with different time constants. Integrating for a longer time, the slow

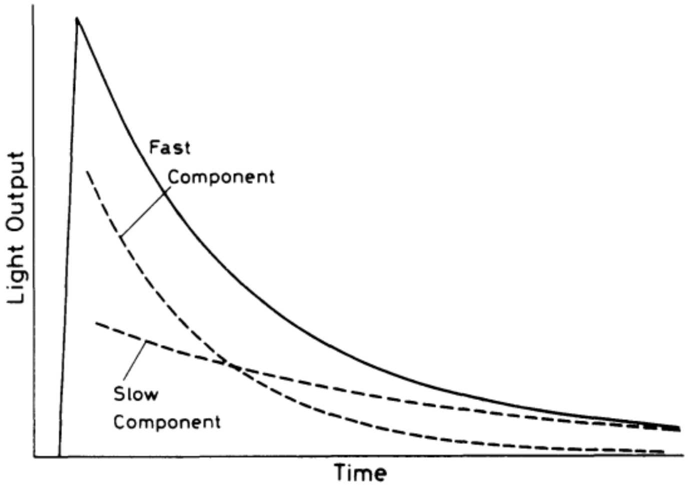

Figure 2.9: Resolving scintillation light into fast and slow components. The solid line represents the total light decay curve.

shaper includes also the fast scintillation contribution consequently correlating the two components. Looking at the fig.(2.5), we can use this method only for the particle (3). An example of a *Fast-Slow* correlation is shown in fig.(2.10) in which is possible to identify the mass number at least up to $Z = 4 - 5$. In the figure, the fast component is reported as a function of the variable ($Slow - 0.9 \cdot Fast$) in order to enhance the isotopic separation between the different lines, by partially decorrelating the two components.

2.4.3 Particle identification procedure

The methods that we used to identify the fragments stopped in the different layers of FAZIA described below, are now summarized:

- PSA (I_{max}) correlation based on Si1 signals to determine Z and A of the fragments stopped inside the first layer up to $Z \simeq 20$;
- $\Delta E - E$ correlation between Si1 and Si2 to identify in Z and A (up to $Z = 25$) the particles stopped inside the second silicon detector;

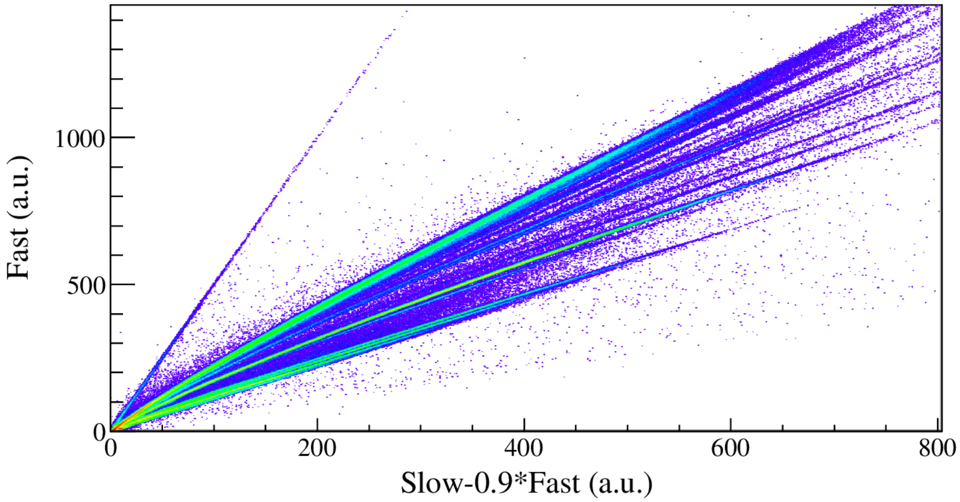

Figure 2.10: Fast-Slow correlation for particles stopped in CsI.

- $\Delta E - E$ correlation between Si2 and CsI to identify in Z and A fragments stopped inside the CsI detector;
- Fast-Slow correlation in CsI to identify in A light particles up to Z = 4-5 stopped inside the CsI detector.

Though the correlation matrices obtained with the techniques listed above differ one from another, the various steps of the identification procedure are common to all the correlations. The first step is the production of an identification grid; starting from the correlation matrix we draw a piecewise linear curve superimposed on a visible experimental curve, corresponding in turn to given A and Z values. In our analysis, in order to obtain better identification using the KaliVeda software, we have generally used only one line for each Z (except for Fast-Slow). An example set of identification lines is shown in fig.(2.11) superimposed on the ($\Delta E - E$) Si1-Si2 matrix. In this figure, we also show the graphical interface, that is divided in 4 icon groups:

- *Trasformation*, allow to select the trasformation that we want to apply to the grid: **rotation** in the z axis (R_Z), **traslation** in the axis x,y (T_X, T_Y) and **scaling** in the

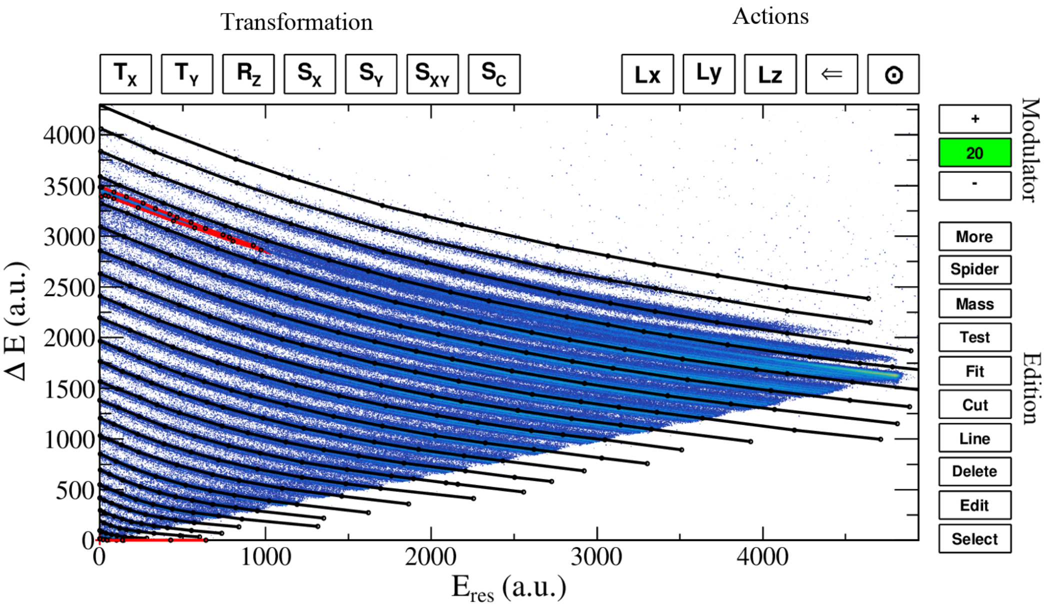

Figure 2.11: Identification grid superimposed on a $\Delta E - E$ matrix correlation Si1-Si2. Show also the KaliVeda graphical interface.

axis x, y simultaneosly (S_{XY}) or separately (S_X, S_Y) and also the scaling of the curvature of the grid (S_C).

- *Modulator*, allow to set the step width of the transformation.
- *Actions*, allow to change the visualization of the grid, setting in the three axis the logscaling (L_X, L_y, L_Z) and unzoom (⊙).
- *Edition*, allow to edit the identification grid adding lines and graphical profile, but also to performe some Test or Fit.

For further detail see ([35], chapter 2).

To each piecewise linear line we assign a number called PID or PI (Particle IDentification parameter) whose value is equal to the atomic number (Z) of the fragments associated to the underlying experimental curve. Graphical contour cuts, in red in fig.(2.11), are used to exclude from the identification procedure some portion of the matrix, i.e.

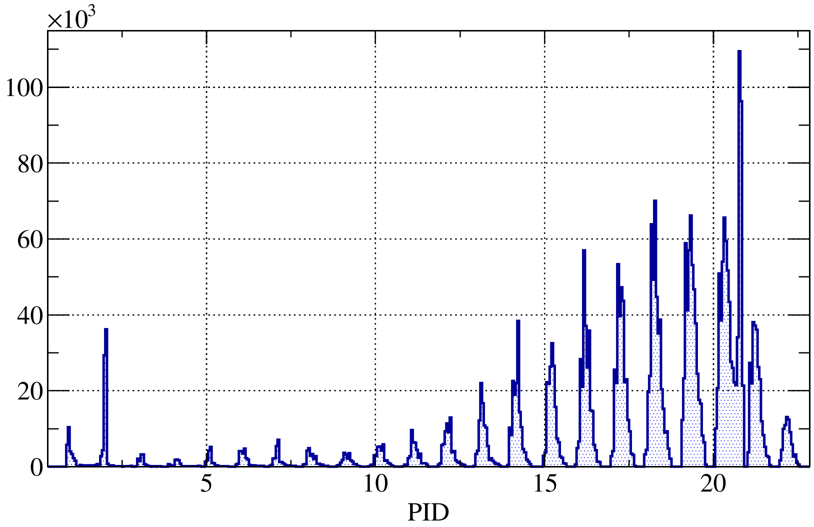

Figure 2.12: PID distribution, made using the grid shown in fig.(2.11).

those inside the area determined by the contour. The excluded events would otherwise contribute to the background or degrade the identification resolution.

During the data analysis, a PID number is assigned to each detected fragment by interpolating between the drawn lines, basing on the event position in the correlation. The interpolation algorithm, implemented in KaliVeda, evaluates the relative distance between the point on the matrix and the 4 closer lines of the grid.

After the interpolation procedure, we obtain a PID distribution as shown in fig.(2.12) where every peak corresponds to a different isotope. The PID distribution shown in fig.(2.12) was obtained using the grid shown in fig.(2.11). The result of the identification procedure that we obtain is shown in fig.(2.13), the nuclide chart (Z Vs. N) for the method $\Delta E - E$ for Si1 and Si2.

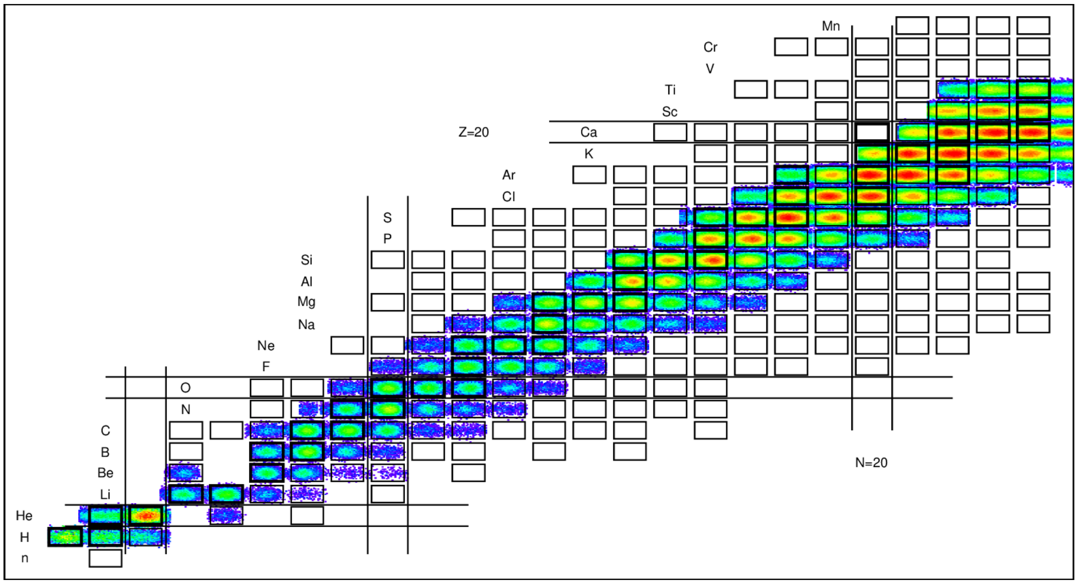

Figure 2.13: Nuclide chart of the particles identified in Z and A, made using the grid shown in fig.(2.11).

Chapter 3

Analysis of the reactions $^{40,48}Ca +^{40,48} Ca$ at 35 MeV/u

The first campaign of INDRA-FAZIA experiments described in chapter 2 has recently finished. The data will be calibrated before being analyzed. For this reason, during my internship at GANIL (21/01-31/05/2019), I have analyzed data of the previous INDRA-VAMOS campaign (*e503*) for the reactions $^{40,48}Ca+^{40,48}Ca$ at 35 MeV/u. The results of the analysis may be very useful for making comparisons between the two experiments. In the INDRA-FAZIA experiments, we expect a less mass resolution but larger angular coverage and the set-up is easier to be analyzed with respect to the experiment with VAMOS.

In this chapter, we will briefly present the INDRA-VAMOS apparatus, the characteristics of the fragments detected in VAMOS and the behavior of the charged products detected in INDRA. The correlation between the two quantities will allow the reconstruction of (Z, A) of primary fragments.

3.1 Overview of INDRA-VAMOS

The experiment was performed at the GANIL facility, where $^{40,48}Ca$ at $E = 35\,MeV/u$ impinged on a self-supporting $1\,mg/cm^2$ ^{40}Ca or $1.5\,mg/cm^2$ ^{48}Ca targets placed inside the INDRA vacuum chamber. The typical beam intensity was around $5 \cdot 10^7\,pps$.

Fig.(3.1) shows a picture of the experimental set-up where can be seen the coupling of the two apparatuses. The charged particle multidetector array INDRA, in the setup used in this experiment, covers the polar angle from 7^o to 176^o, to allow the coupling with the VAMOS spectrometer in the forward direction. Rings 4 to 9 ($7^o - 45^o$) are composed of 24 three-layer detection telescopes: a gas-ionization chamber, a 300 or 150 μm silicon wafer and a CsI(Tl) scintillator (14 to 10 cm thick) read by a photomultiplier tube. Rings 10 to 17 ($45^o - 176^o$) are composed of 24, 16 or 8 two-layer telescopes: a gas-ionization chamber and a CsI(Tl) scintillator of 8, 6 or 5 cm thickness. Fragment identification thresholds are around 0.5 and 1.5 MeV/u for the lightest ($Z \simeq 10$) and the heaviest fragments, respectively.

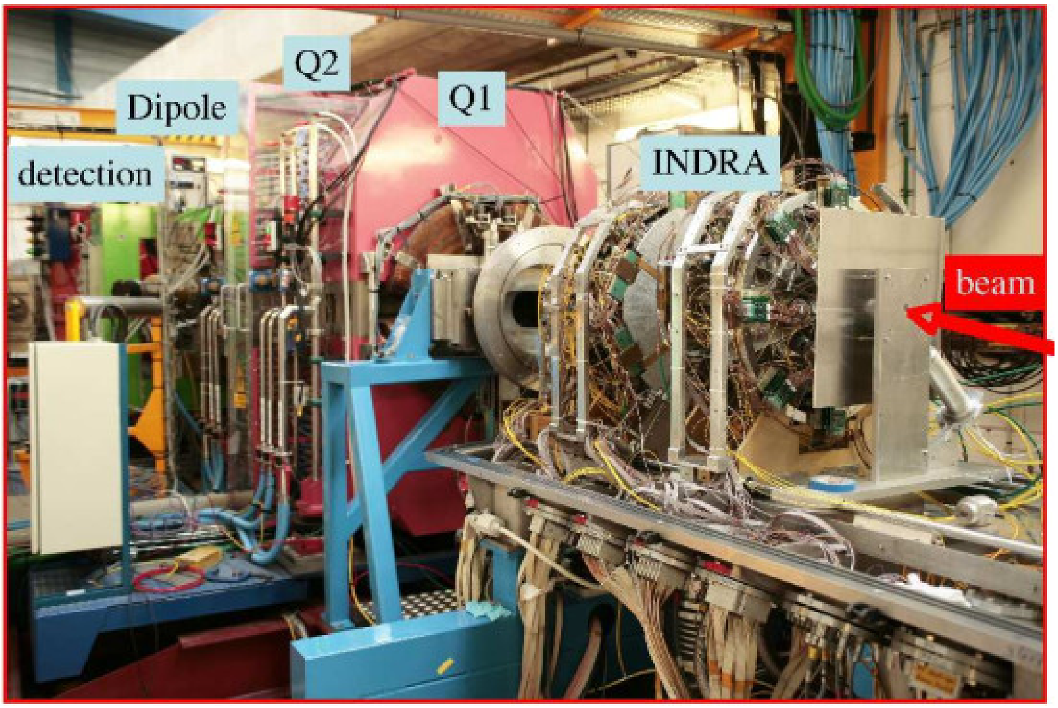

Figure 3.1: A picture of experimental setup of INDRA-VAMOS coupling.

The VAMOS spectrometer is constituted by two large magnetic quadrupoles focussing the incoming ions in the vertical and horizontal planes, followed by a *Wien filter* (not used in this experiment) and a large magnetic dipole, which bends the trajectory of the

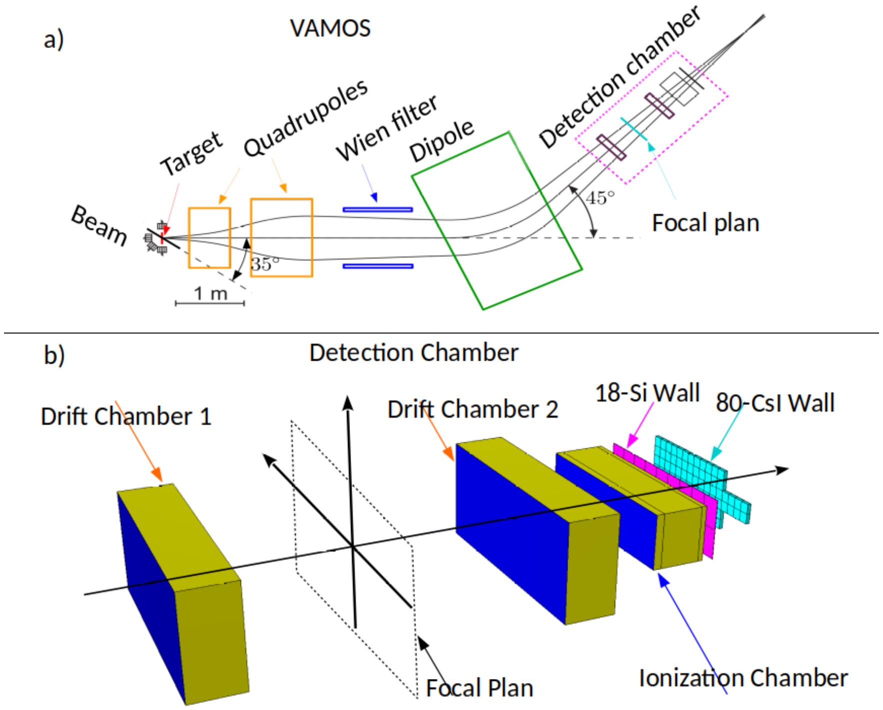

Figure 3.2: a) Representation of the VAMOS optical line. In this example the spectrometer was rotated at 35^o with respect to the beam axis and the detection plane was set at 45^o with respect to the reference trajectory. b) Global 3-dimensional view of the detection chamber. The reference frame used is that of the reference trajectory.

ions.

Fig.(3.2.a) shows VAMOS optical line. In the present setup, the spectrometer covers the forward polar angle from 2.5^o to 6.5^o, with an acceptance of $\theta \simeq \pm 2^o$, thus allowing the detection of PLF emitted slightly above the grazing angle of the projectile. The momentum acceptance is about ±5%. The focal plane is located $9\,m$ downstream. This time of flight base allows a good resolution of the identification of all isotopes produced in this experiment. Fig.(3.2.b) shows a 3-dimensional global view of the detection chamber located in the focal plane of VAMOS. It is composed of two drift chambers, which give the position of the reaction products, followed by a sandwich of detectors: an ionization chamber (7 modules), $500\,\mu m$ thick Si-wall (18 independent modules) and

1 *cm* CsI-wall (72 detectors). Several magnet rigidity ($B\rho$) sets of the spectrometer were measured for each system to cover the full velocity range of the fragments.

At least one hit on the VAMOS Si-wall was required for each event to be acquired, thus selecting semi-peripheral and peripheral collisions as well. Other trigger configurations, allowing to select more central collisions, were set but will not be discussed in the present work.

3.2 Characteristics of fragments

In order to characterize the origin of the reaction products detected in VAMOS we show in fig.(3.3) an overview of the events for the reaction $^{48}Ca +^{48} Ca$. Here in left panel, we present the fragment charge detected in the VAMOS focal plane (Z_{vamos}) as

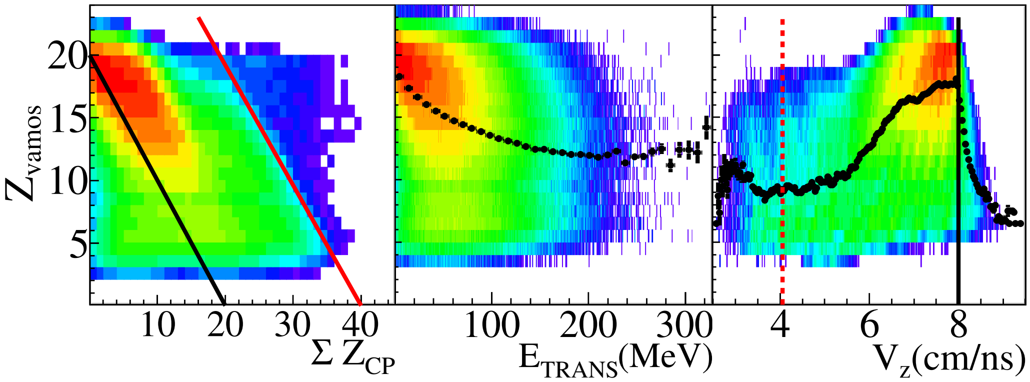

Figure 3.3: Atomic number of the fragments detected in VAMOS focal plan (Z_{vamos}), for ^{48}Ca+^{48}Ca system, as function of three variables: i) (left panel) the sum of atomic number of particles collected with INDRA, the lines indicate a complete charge detection of the total system, $Z_{proj} + Z_{target} = 40$ (red line) and charge conservation for projectile $Z_{proj} = 20$ (black line); ii) (center panel) total transverse energy of LCP (E_{TRANS}) detected in INDRA, the symbols represent the average value of Z_{vamos} per E_{TRANS} bin; iii) (right panel) the parallel velocity in the laboratory frame of the fragment detected in VAMOS, the dashed vertical line indicates the c.m. velocity of the reaction and solid vertical line corresponds to the projectile velocity, respectively, the black symbols represent the average value of Z_{vamos} per velocity bin.

a function of the sum of the particle charges collected with INDRA (ΣZ_{CP}). The lines indicate the total detected charge ($\Sigma Z_{CP} + Z_{vamos}$): the black line is equal to the charge of the projectile ($Z_{proj} = 20$) and the red one is the total system charge ($Z_{system} = 40$). Most of the events are located around and beyond the line that conserves the charge of the projectile. This indicates a good detection efficiency of the forward emitted quasi-projectile (*QP*) and a well performing correlation between the two devices. For a fraction of the events a complete detection of all reaction products is achieved. One can observe also the low background exceeding the total charge of the system. These events are attributed to pile-up of signals.

In order to estimate the degree of dissipation of the reaction, we have chosen the sum of transverse energy (E_{TRANS}) of light charged particles (*LCP*, $Z = 1, 2$), as an impact parameter selection, defined as:

$$E_{TRANS} = \sum_{Z=1,2} \frac{p_\perp^2}{2m} \tag{3.1}$$

where the summation is taken over the particles with $Z = 1, 2$ only, and $p_\perp$ and m are the linear momentum component perpendicular to the beam axis and mass of each of these particles, respectively. This global observable is suitable for collisions from peripherals to semi-peripherals and the data because INDRA detector is very efficient ($\simeq 90\%$) for the detection of LCP [36]. Indeed, in the central panel of fig.(3.3) we present Z_{vamos} as a function of E_{TRANS}, one can see a strong correlation with fragments having $Z_{vamos} > 12$ and a saturation around $Z_{vamos} = 10$. An estimation of the corresponding impact parameter b has been done exploiting AMD model calculation. The simulated events has been filtered by the experimental acceptance. As expected, the most important selection is made by the VAMOS acceptance which select mainly from the peripheral to semi-peripheral collisions. The deduced impact parameter is in the range of $b = 5 \div 8.2\, fm$. The most of the cross section is associated with the fragments with the charge range $Z = 12 \div 20$.

Finally, in the right panel, we show Z_{vamos} as a function of their longitudinal velocity in the laboratory frame (V_Z). The spectrometer covers a forward polar angular range

$\theta = 2.5^o \div 6.5^o$, and the $B\rho$ setting of the spectometer allows to cover a velocity between the projectile and the center of mass velocities, $4 \leq V_Z \leq 8\,(cm/ns)$. The fragments detected in VAMOS come mainly from a quasi-projectile (QP) with a low contamination of the quasi-target (QT), and a lower contribution from the mid-rapidity zone is also present. The average value of the charge distribution superimposed in the distribution of fig.(3.3) shows significant correlation between the velocity of the fragments and their charge. On average, slower fragments are associated with smaller charges. The above observations suggest that the fragments detected in VAMOS are compatible with dissipative binary collisions, and they are the products of the quasi-projectile decay resulting from peripheral collisions. The decrease in the average velocity is associated with an increase in excitation energy, which implies a smaller evaporation residue. Slower and lighter fragments are also produced, emitted by the neck at mid-rapidity. As expected an high production is observed when the charge and velocity are close to those of the projectile, $6 \leq V_Z \leq 8\,(cm/ns)$.

In conclusion, what we can see from the fig.(3.3) is that the four variables are strongly correlated and the highest data concentration is given for $Z_{vamos} \geq 12$, with properties similar to those of the projectile. This is why, in the following, we will call them *Projectile-like fragment (PLF)*.

3.2.1 Neutron excess

It is important to study the evolution of the average neutron excess ($< A > -2Z$) of the fragments detected in VAMOS as a function of their atomic number for the four systems under study, see fig.(3.4), in order to understand some of the various mechanisms involved during the reaction process. We observe a matching of the evolution of the curves according to the neutron content of the projectile: as expected, the fragments produced with ^{48}Ca projectile are more neutron-rich than those with the ^{40}Ca projectile. However small effect of the target is visible in the figure (open symbols). This sensitivity to the target may indicate the isospin diffusion mechanism.

In the same figure we have plotted the *Evaporation Attractor Line* (EAL), using the

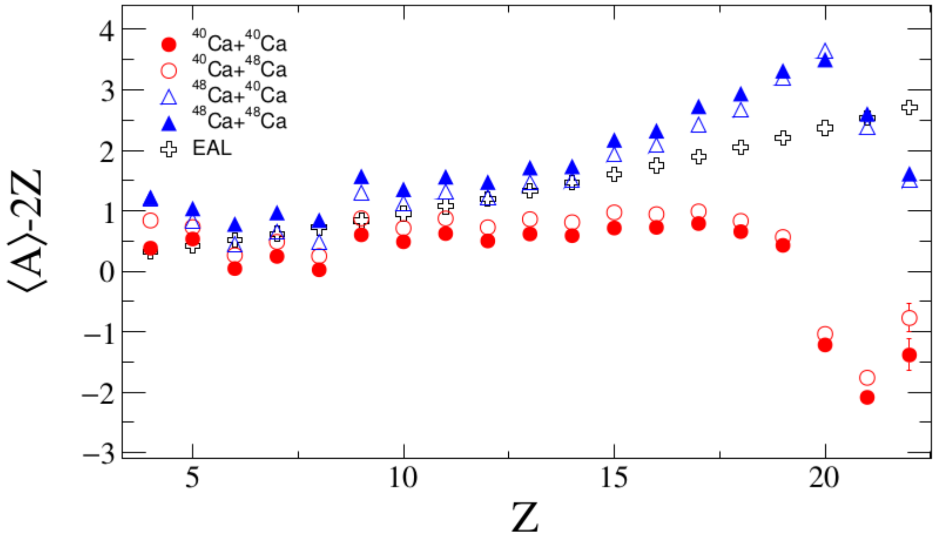

Figure 3.4: Distribution of the average neutron excess $< A > -2Z$ of the fragments detected in VAMOS as a function of their atomic number for the four systems $^{40,48}Ca +^{40,48} Ca$ at $E/A = 35\,MeV$. The empty cross symbols are a result of simple EAL parametrization, for more details see text...

parametrization shown in eq.(3.2). Let us first recall the EAL [37]. In nuclear reactions, one or more excited primary fragments are formed which decay by evaporation of nucleons and light clusters. This evaporation process can substantially alter the proton-neutron asymmetry of the initial primary fragments. What was noted is that at sufficiently large excitation energies, independent of the assumed Z and A of the primary fragments, evaporation models predict that the average location of the secondary fragments in the chart of nuclides is always close to a particular line. The location of this line is mainly determined by competition between proton and neutron evaporation. This line thus acts as if it is attracting the decaying systems and it is called the evaporation attractor line (EAL). A good approximation, for $Z < 90$, is:

$$Z = 0.909\,N - 1.12 \cdot 10^{-3} N^2\,. \tag{3.2}$$

Concerning the distributions of the neutron excess, we observe for $Z = Z_{proj} = 20$, that the ^{48}Ca projectile systems have a neutron excess of 3.5 that has to be compared to the initial one that is 8. The 4.5 neutron loss can be explained by neutron transfer reactions between the projectile and target, but also the decay of an excited projectile preferentially by neutron emission. Indeed, at low excitation energy of a nuclei, the most probable exit channel is the neutron evaporation process. Then as we move away from the charge of projectile the neutron excess decreases and the distributions approach the (EAL). This may reflect an increasing projectile excitation with the reduction of the charge of the quasi-projectile. Finally, for the ^{40}Ca projectile systems, we observe that for $Z = Z_{proj}$ the fragments present a deficit of 1.5 neutrons, this deficit quickly decreases with the charge of the QP and again the distributions approach the EAL from the neutron deficient side.

In case of the *pickup process* ($Z > Z_{proj} = 21-22$), for neutron rich systems the addition of two charges decreases the neutrons excess while for the neutron poor the deficit is less important than for the *stripping process*[1].

3.3 Characteristics of LCP

As we described in sec.(1.1.1), the initial dynamics of heavy-ion collisions at intermediate energy are complex. During the interaction the projectile and target nuclei exchange few nucleons and then re-separate, keeping some memory of the entrance channel. The remnant of the two nuclei (quasi-projectile QP and quasi-target QT) evolve into moderately excited nuclei which decay by emitting light particles. The evaporated particles are correlated with the fragments from which they were originated. Their energies, with respect to the fragment, are characteristic of evaporation. The relative velocities between the particles and the detected fragments inform us about the nature and origin of the particles. It is possible, experimentally, to associate light particles with a

---

[1] Processes with exchange of nucleons between target and projectile are called: *pickup* when there is the exchange from the target to the projectile and *stripping* from the projectile to the target.

fragment and to determine the degree of excitation of the latter. Thus, in peripheral collisions, binary reactions take place while the QP is de-excited in a large fragment called PLF and some light particles. In semi-peripheral collisions, the QP breaks up into two or more excited heavy fragments. The de-excitation of these fragments will lead to the emission of a large fragment with the emission of some charged particles and clusters. In the following, the parent nucleus of the PLF will be referred to as primary fragment and the evaporated particles as particles emitted in coincidence.

One of the aim of this work is to determine the intrinsic properties of the primary fragments produced in peripheral and semi-peripheral collisions. In this section we present the method which allows us to associate the evaporated LCP and PLF to a given *primary fragment*.

3.3.1 Multiplicity study

The multiplicities of light particles detected in INDRA, are important since the reconstruction of the primary fragment is strictly correlated to this observable. We restricted our study to the forward part of the center of mass frame, the angular region for which INDRA has the best quality of isotopic identification. Fig.(3.5) shows the average multiplicities of light charged particles detected in INDRA as a function of the fragment collected in VAMOS. We first note some global trends of the average multiplicities independent from the systems: they increase as the PLF charge decreases, reflecting increasingly dissipative collisions (the centrality of the collisions) and as well an increasingly excited system; a saturation at lower charges is present.

Secondly, we observe some general trends by comparing the systems, especially for nuclei with neutron deficiency or enrichment. The protons and ^3He (neutron deficient) but also the tritons and ^6He (neutron-rich) show average multiplicities which depend on the N/Z of projectile and target. Thus, for the same neutron-rich nucleus, the hierarchy of multiplicities follows that of the N/Z of the projectile and then of the target and vice versa for the neutron-deficient systems.

Thirdly, the multiplicities of the deuteron and ^4He, particles having the same number

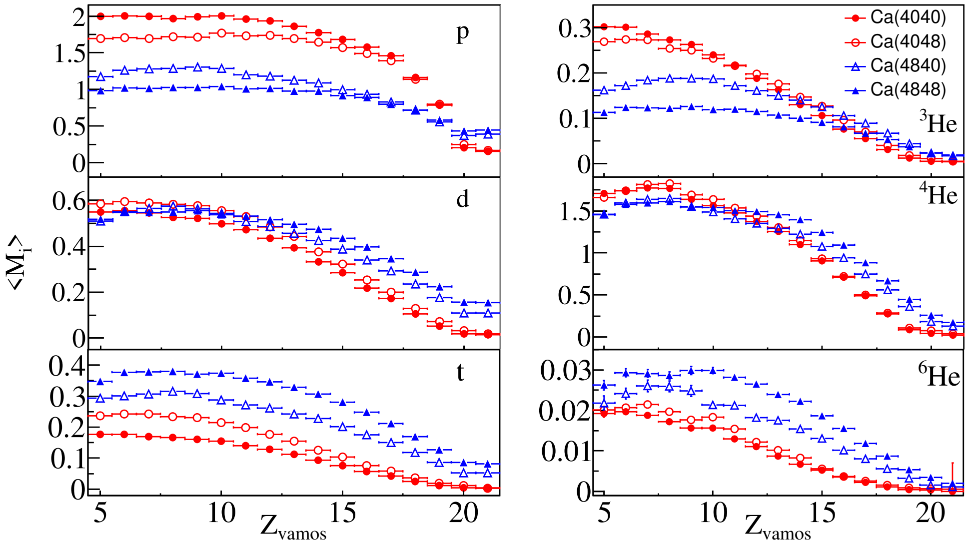

Figure 3.5: Average LCP multiplicity detected in INDRA based on fragment load detected in VAMOS.

of protons and neutrons, have different trend than the previous observations and their multiplicities depend much less on the system. Thus for the deuterons (respectively the ^4He) the multiplicities are paired according to the nature of the projectile for high charges and saturate around 0.6 (respectively 1.5) from $Z \sim 10$. It is interesting to note that the multiplicities of the protons , tritons and $^{3,6}He$ show a dependence of the nature of the projectile for the high charge and are higher for the projectiles of ^{48}Ca. This does not reflect for example the *Q-value* associated with the emission of a particle α by the initial projectile: we have indeed $Q_R = -13.97\ MeV$ for the emission of an α by the projectile of ^{48}Ca against $Q'_R = -7.04\ MeV$ for the ^{40}Ca, showing that a statistical emission of an α is more favorable for the ^{40}Ca projectile this is not observed experimentally and highlights some dynamic effects.

3.3.2 Selection of emitting sources

Only peripheral and semi-peripheral collisions, leading to a heavy QP residue with $Z > 5$ detected in VAMOS, are discussed therein. To reconstruct the charge (Z_{QP}), mass (A_{QP}) and momentum vector ($\vec{p}_{QP}$) of the QP, particles detected by INDRA with ($Z = 1, 2$), were attributed to QP decay when their longitudinal velocities are within the limits of $V_{//}^{CM} > 1\,(cm/ns)$ for hydrogen isotopes and $V_{//}^{CM} > 1.5\,(cm/ns)$ for $Z = 2$ isotopes, of the coincident QP residue velocity [?]. This selection is intended to remove fragments from the mid-rapidity and other non-QP sources. Fig.(3.6) (upper panels)

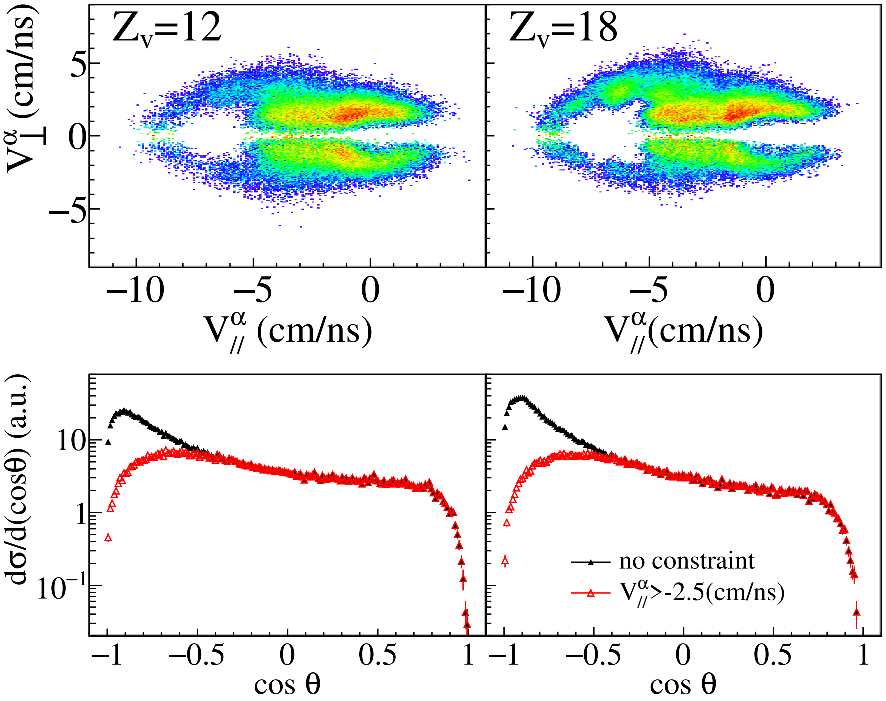

Figure 3.6: $V_{//} - V_{\perp}$ map (top panels) of α particles detected in coincidence with the isotopes of $Z_{PLF} = 12$ (left) and of $Z_{PLF} = 18$ (right) represented in the reconstructed center of mass frame of the quasi-projectile (QP). Associated angular distributions (bottom panels) of α in the QP center of mass frame, with no kinematical constraints(black filled symbols) and with $V_{//}^{\alpha} > -2.5\,(cm/ns)$ (red empty symbols).

shows the invariant parallel versus perpendicular velocity in the QP center of mass frame of α particles ($V_{//}^{\alpha} - V_{\perp}^{\alpha}$) detected in coincidence with the isotopes of $Z_{PLF} = 12$ (left panel) and $Z_{PLF} = 18$ (right panel). The kinematic reconstruction of the QP center of mass takes into account the reaction plane by rotating the event accordingly.

In doing so, for fragments of a given (Z, A), having different emission angles in the center of mass, the procedure enables to construct a common reference frame for the LCPs in coincidence with these fragments. The two main components drawing circular regions akin to Coulomb ring can be clearly seen. One component, centered on the origin $(0, 0\,[cm/ns])$, can be attributed to the PLF parent and the second component at $(-8, 0\,[cm/ns])$ to the TLF parent ($-8\,(cm/ns)$ value corresponds to the velocity of the QT in the QP center of mass frame).

In addition to the two sources, we observe a superposition of a third contribution at mid-rapidity around $V^{\alpha}_{//} = -4\,(cm/ns)$. More precisely, the third emitting source is visible at $-4.5 < V^{\alpha}_{//} < -2.5\,(cm/ns)$. This is the first time that the mid rapidity source is evidenced in this Fermi energy domain. Thanks to the high resolution of the velocity provided by VAMOS, it was possible to make this observation. See fig.(3.7).

The impact of these velocity selections is investigated in bottom panels of fig.(3.6),

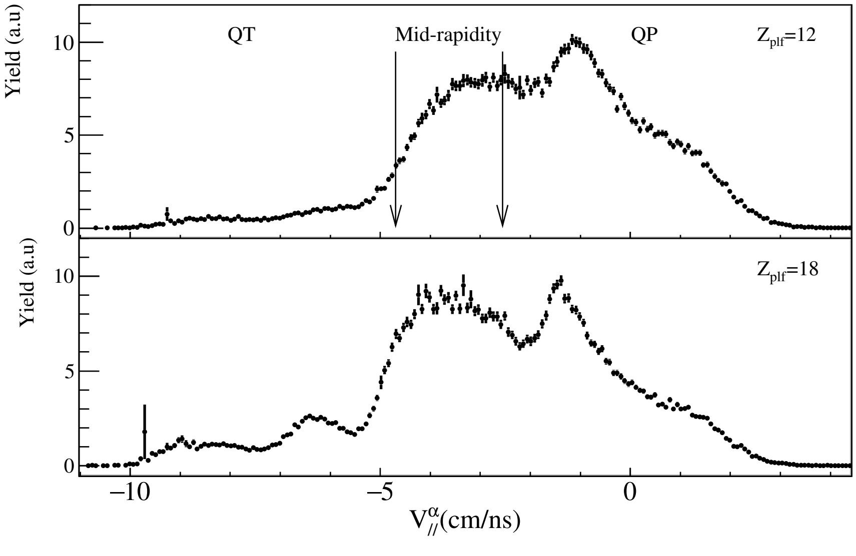

Figure 3.7: $V^{\alpha}_{//}$ distributions for Z_{PLF}=(12,18). We can distinguish three emitting sources, the separation is highlighted by the two arrows in the upper panel: *QP* has $V^{\alpha}_{//} \geq 2.5\,(cm/ns)$, *QT* has $-4.5 \leq V^{\alpha}_{//}\,(cm/ns)$ and the *mid-rapidity* has $-4.5 < V^{\alpha}_{//} < -2.5\,(cm/ns)$.

that shows the angular distributions in the frame of alpha particles with *i)* no kinematical constraint, *ii)* $V^{\alpha}_{//} > 1.5\,(cm/ns)$. For the first case, the angular distributions are almost flat up to $cos\theta > -0.3$ and then they increase toward backward angle to be peaked at $cos\theta = -1$. This increase vanishes when introducing the constraints, which minimize the contribution of the TLF and sources other than the PLF. The flattening of the angular distributions should indicate an isotropic emission from the PLF parent nucleus. Obviously the angular distributions observed are not flat. The diminution of the yield observed at small angles $cos\theta > 0.8$ is due to non-detection of the emitted LCP in the cone ($0^o \div 7^o$), where VAMOS is placed.

The observed anisotropy can be ascribed to two causes: a not-negligible angular momentum of the parent nucleus and the bias introduced by the fact that the PLF is detected only on one side of the beam axis. The possible angular momentum would favor a forward-backward emission of the particles and a depletion at 90^o. To investigate the anisotropy induced by the angular momentum, we performed statistical calculations with the GEMINI code. ^{48}Ca nuclei with $E^*/A = 3\,MeV$ and angular momentum varying from 0 to $60\hbar$ were deexcited by the code and filtered with an experimental filter, see fig.(3.8). The experimental filter accounts for the geometry and energy thresholds of the INDRA detector, and for the geometry and velocity acceptance of the VAMOS detector. The best agreement between the experimental and simulated angular distributions was found for $J = 0\hbar$ angular momentum. This result is in agreement also with molecular dynamics calculation (AMD) predictions for the studied systems, which predict an angular momentum distribution of forward emitted parent nuclei rather broad (up to $60\hbar$) but peaked at small J values. We therefore conclude that the distortion observed in the angular distributions is mainly due to the detection of the PLF in one side of the beam.

3.4 Reconstruction of primary fragment

The velocity selection method, described in the previous section, was applied, event by event, to LCP (p, d, t, ^3He, α and ^6He) emitted in coincidence with PLFs. In the

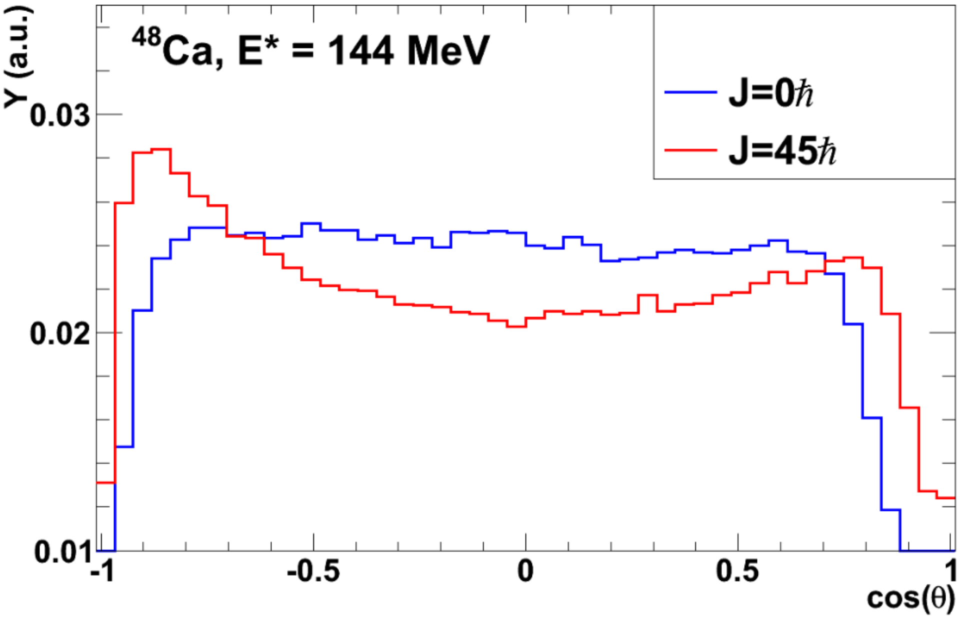

Figure 3.8: Filtered GEMINI simulations for angular distributions in the PLF center of mass reference for alphas for the de-excitation of a ^{48}Ca nucleus to a 144 MeV excitation energy with two angular momentum values.

following, it will be implicit that the considered LCP were accepted by our velocity selection.

In this section, we reconstruct the charge and the mass number of the primary fragments.

3.4.1 Primary fragment charge

The primary fragment charge (Z_{pr}) is reconstructed as the sum of the PLF charge and the evaporated LCP charges in the event, asking at least one particle in INDRA in coincidence with the fragment detected in VAMOS.

Z_{pr} is then given by the relationship:

$$Z_{pr} = Z_{PLF} + \sum_{i=1}^{M_{LCP}} z_i \tag{3.3}$$

where z_i is the charge of the evaporated particle i, runs over all LCP multiplicities.

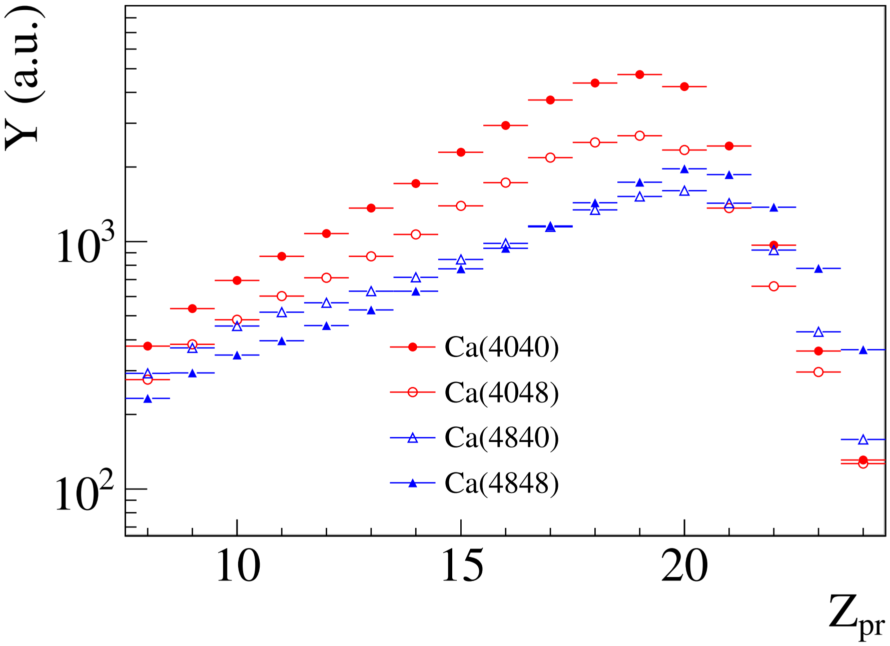

Figure 3.9: Reconstructed primary fragment charge (Z_{pr}) distributions of $^{40,48}Ca +^{40,48} Ca$ systems.

Fig.(3.9) shows the charge distributions of primary fragments for the four systems. The distributions are peaked at $Z_{pr} \sim 20$ and populate charges ranging from 8 to 25. The trend of the distributions doesn't have significant differences between the different systems. What we can observe is that when the centrality of the collisions increases, the distributions of the system $^{40}Ca +^{48} Ca$ and $^{48}Ca +^{40} Ca$ merge at the same value. This might indicate an equilibration between both systems (for $Z = 8 - 10$).

In order to test the quality of the reconstruction of primary fragments, we will study the even-odd staggering, which can be attributed to the signature of the effects of the nuclear structure at low excitation energies. However, for intermediate energy collisions, the structural effects are restored in the production of the final fragments during the disintegration of the hot fragments and that the even-odd staggering depends on the structure of the nucleus produced near the end of the chain of decays [38].

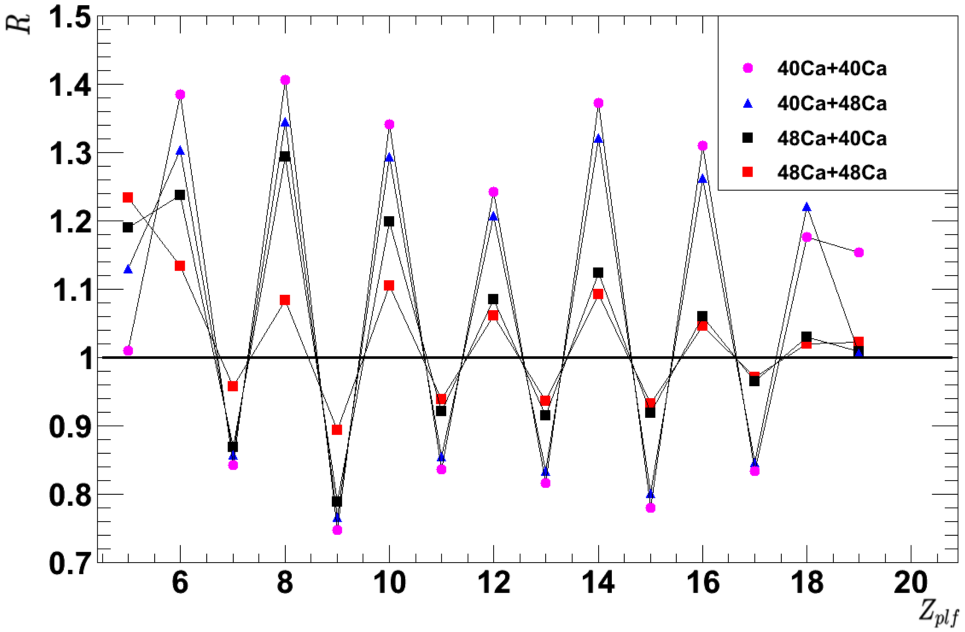

Figure 3.10: Ratio between the fragment yield Y(Z), as measured in VAMOS, and smoothed values $Y_{smooth}(Z)$ as a function of the fragment atomic number. Statistical errors are smaller than the symbol sizes.

To study this odd-even effect, we determine the ratio of experimental production rates $Y(Z)$ and a smoothed value of this yield $Y_{smooth}(Z)$ for five consecutive points (Z and $Z \pm 2$). This ratio amplify the odd-even staggering. Fig.(3.10) shows the ratio of production rates to adjusted values for PLF charge distributions and for different systems. The $R(Z)$ ratios oscillate around 1 (continuous line) with even-odd staggering. The staggering values are high, varying between 10 and 40% depending on the system studied. These values depend on the neutron richness of the system and staggering is less important for higher neutron-rich systems. For the region between $Z = 11$ and $Z = 20$, the influence of the projectile is manifest. We find systems with a ^{48}Ca projectile with lower values compared to systems with a ^{40}Ca projectile.

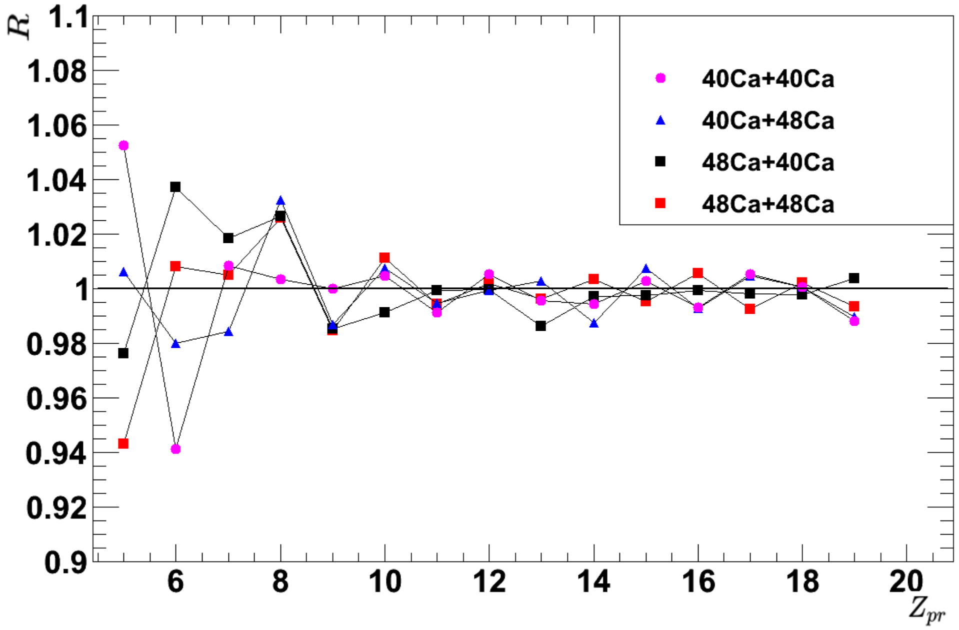

Figure 3.11: Same as fig.(3.10) for the yield of the reconstructed primary fragments. Notice the zoom applied to R-axis scale.

The same study can be done for the primary charges. Fig.(3.11) shows the ratio for primary charge distributions and for different systems. Lower staggering values are found, around 6% for charges less than 10, and values around 1% for charges greater than 10. For lower Z_{pr}, the reconstruction is wrong since we do not detect lower charges. Here the side effects are very strong and therefore, in the following, we will consider only primary fragments with charge $Z_{pr} > 9$ to be safe.

3.4.2 Primary mass number

We define the distribution of the primary mass number without evaporated neutrons, $A_{prwon}(Z_{pr})$, as the sum of PLF mass and charged particle masses for a given primary charge,

$$A_{\text{prwon}}\left(Z_{pr}\right) = A_{PLF}\left(Z_{pr}\right) + \sum_{i=1}^{M_{LCP}} a_i \tag{3.4}$$

where a_i is the mass number of detected LCP. This reconstruction is done event by event. In this equation, if one adds the multiplicity of emitted neutron (M_n , not measured), one obtains $A_{pr}(Z_{pr}) = A_{prwon}(Z_{pr}) + M_n$. Fig.(3.12) shows the distribution of the primary masses without the contribution of neutrons for the different systems. A dependence in function of the projectile is observed, where maximum values of primary A_{prwon}=55 is observed, that correspond to an increase of the 13% if we consider ^{48}Ca. As we said for the Z_{pr} distribution, when the centrality of the collision increases, the distribution of the systems $^{40}Ca +^{48} Ca$ and $^{48}Ca +^{40} Ca$ converge at the same value.

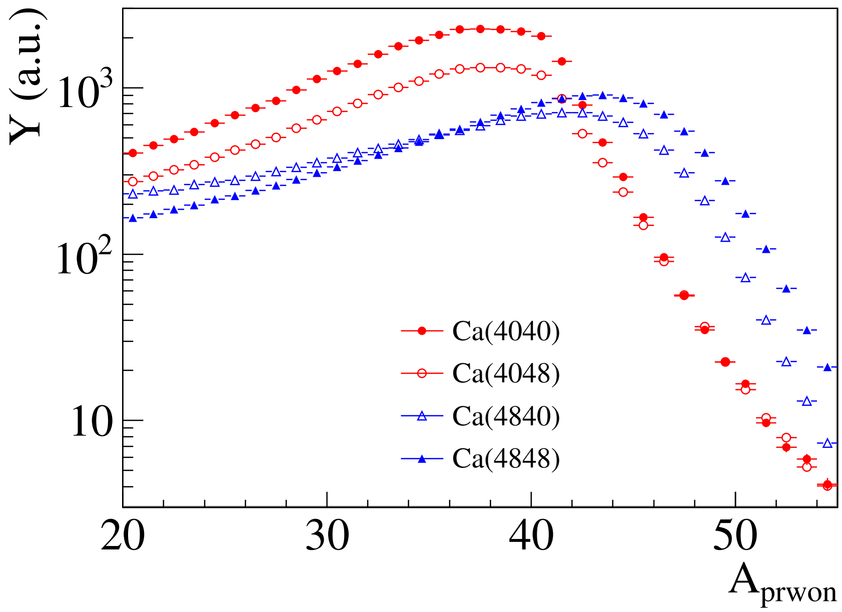

Figure 3.12: Reconstructed primary mass distributions without the contribution of neutrons (A_{prwon}) of $^{40,48}Ca +^{40,48} Ca$ systems.

Chapter 4

Comparison with models and study of symmetry energy

The aim of the previous chapter was to present the experimental data and to show how we reconstruct the primary fragments. In this chapter, we present a comparison of these results with the simulations of the considered reaction to check the validity of the reconstruction. To make the simulation two steps are required: first of all, we have to simulate the nuclear reaction itself and then the de-excitation process which brings the initially excited fragments towards the ground or low-lying states. For the description of the dynamical phase, we adopted the AMD model [39], one of the most accredited at Fermi energies. As fragments produced in the collisions are excited, to simulate the particles evaporation and their statistical fission, we adopted as afterburner the statistical model GEMINI++ [40]. These simulated events have been filtered via a software replica of the apparatus, including the efficiencies, the resolutions and the identification thresholds of the various detectors.

Then we will show the estimation of two observables that required some assumptions: the excitation energy and the temperature of the fragment. Then making the correlation between these two observables we can have the *caloric curve*.

Finally, in the last part of the chapter, we will show the results of the study made to calculate the energy symmetry term of the nuclear equation of state.

4.1 Isotopic distribution

Fig.(4.1) (black dots) show the isotopic distributions of A_{prwon} for Z_{pr} = (12, 14, 18, 20) produced in the $^{48}Ca +^{48} Ca$ system. The fragments predicted by AMD calculation are considered as primary excited fragments. They were utilized as input to statistical model GEMINI in order to estimate the evaporated neutrons and then remove the neutron contribution from A_{pr}. The calculation has been filtered by experimental filter of

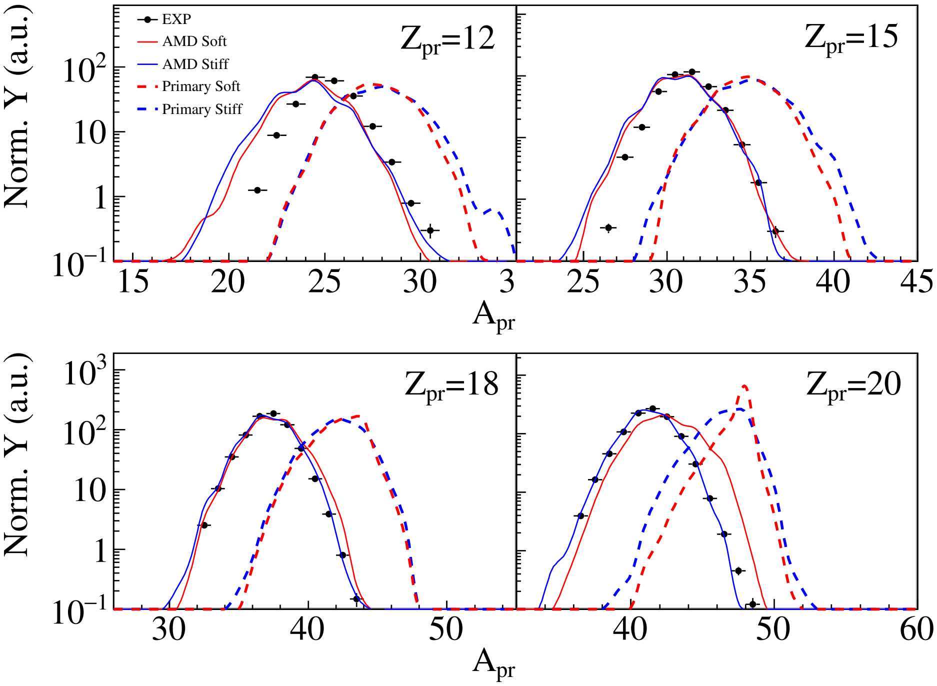

Figure 4.1: Comparison of the primary isotopic distributions without neutron contribution for Z_{pr} = (12, 15, 18, 20) of $^{48}Ca +^{48} Ca$ system. The experimental data are presented by the black symbols, the results of AMD calculation are presented by dashed lines and solid lines indicate AMD simulation without neutron contribution, estimated with Gemini calculation; the blue ones are made using AMD-Stiff and the red ones with AMD-Soft.

VAMOS which is mainly geometrical according to the experimental input window. We also took into account the experimental thresholds of the detectors located in the focal plan. For INDRA, we applied experimental filter which takes into account the geometry and energy threshold of all detectors. We have kept only primary fragments whose final products pass through the experimental filter. The result of this calculation is shown in fig.(4.1) (dashed lines) for primary isotopic distributions and the same without neutrons contribution (solid lines). The latter distributions have been obtained from the isotopic distribution of primary fragments predicted by AMD for which we subtracted the neutrons originating from secondary decay provided by GEMINI calculation. This subtraction of neutrons is done event by event so that the primary mass minus neutrons can be compared directly to the experimental A_{prwon} distributions. One can see in

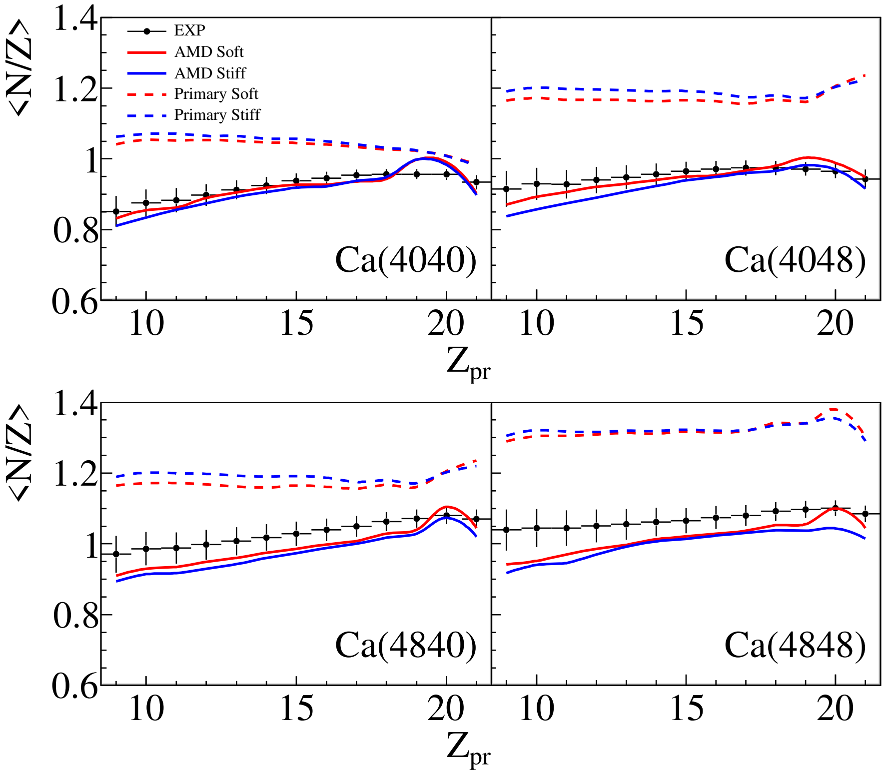

Figure 4.2: Comparison of the primary <N/Z> distributions without neutron contribution for the $^{40,48}Ca +^{40,48} Ca$ systems. The symbols are the same of fig.(4.1).

fig.(4.1) that the experimental primary fragments without neutron contribution, A_{prwon}, for higher charges are very well reproduced by *AMD-Stiff* while discrepancies at the n-poor side for lower charges are observed. The calculated primary isotopic distributions are shifted towards a larger masses.

Fig.(4.2) shows a comparison of the resulting average ratio <N/Z> versus the charge of primary fragments for the four systems under study. Here again we observe a good reproduction of the experimental <N/Z> values by the predicted AMD without neutron contribution. For this observable, between the two calculation AMD-Soft and AMD-Stiff we don't see any significant differences.

This new observable A_{prwon} seems to be interesting since it can be compared directly to the dynamical calculation with a limited assumption on the decay of the excited primary fragments. This assumption correlates with removing only neutrons estimated with a statistical calculation from the original isotopic distribution predicted by dynamical calculation. However, to determine the excitation energy it is necessary to estimate the neutron emitted during the decay phase of the reaction. Since we do not measure experimentally the emitted neutrons, some assumptions have to be made. This will be discussed in the next section.

4.2 Excitation energy

We can determine the excitation energy of the reconstructed primary fragments, using the following relation:

$$E^{*} = \sum_{i} M_i E_k^i + Q \tag{4.1}$$

where E^{*} is the excitation energy of the source, M_i is the multiplicity of light charged particles ($Z = 1, 2$), E_k^i is the kinetic energy of light charged particles and Q is the mass excess of the reaction defined as the mass of the reconstructed source without the neutrons minus the mass of the emitted particles. However, since the primary fragments are reconstructed without the contribution of the neutrons, the extracted excitation energy values do not correspond to reality. We can nevertheless analyze the general form of the distribution. This quantity also gives us an idea of the degree of dissipation of the collision.

Fig.4.3 shows the excitation energy per nucleon for the four systems under study. We

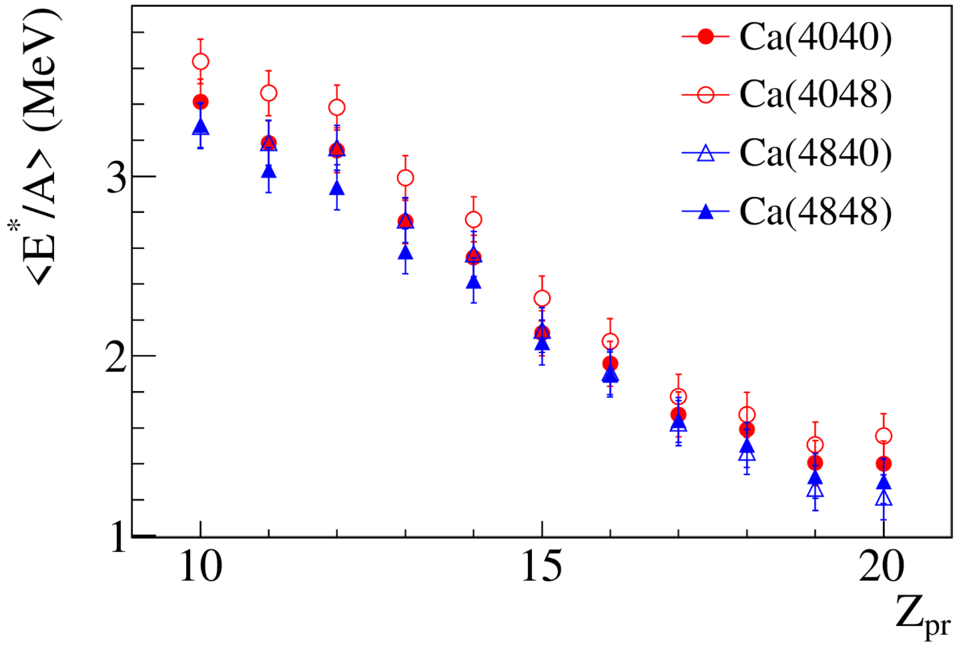

Figure 4.3: Average of the excitation energy per nucleon for the four systems under study. This values are calculated without the contribution of the evaporated neutrons.

first note that the excitation energy distributions have a minimum for higher charge. This is due to the fact that the fragments close to the projectile exchange few nucleons with the target and therefore less dissipation. As one moves away from the projectile more nucleon transfers occur, thus increasing the excitation of the projectile. We also see that calculated excitation energy is lower for neutron-rich systems than for neutron-poor systems. This can be explained by the fact that neutrons are not taken into account in the calculation of excitation energy affects neutron-rich systems more than neutron-poor systems. Therefore, the excitation energy of neutron-rich systems can be higher if neutrons are taken into account.

We now make an assumption about the number of evaporated neutrons, we consider the following relation that conserve the mass number of the reaction:

$$N_{evaporated} = Z_{pr}\left(1 + \frac{n}{z}\right) - A_{prwon} \tag{4.2}$$

where $n/z = 1.40$ for the ${}^{48}Ca +{}^{48} Ca$ system, 1.30 for the ${}^{48}Ca +{}^{40} Ca$ system, 1.10 for the ${}^{40}Ca +{}^{48} Ca$ system and 1.00 for the ${}^{40}Ca +{}^{40} Ca$ system. For the symmetric systems ${}^{40}Ca +{}^{40} Ca$ and ${}^{48}Ca +{}^{48} Ca$, on average, n/z should reflect the N/Z of the system, which is also equivalent to that of the projectile or target. For ${}^{48}Ca +{}^{40} Ca$ or ${}^{40}Ca +{}^{48} Ca$ systems, we consider that the neutron transfer between the target and the projectile does not reach equilibrium in n/z at Fermi energies where the reaction times are short. Thus, the value of 1.30 is set for the ${}^{48}Ca+{}^{40} Ca$ system (instead of 1.20 if the

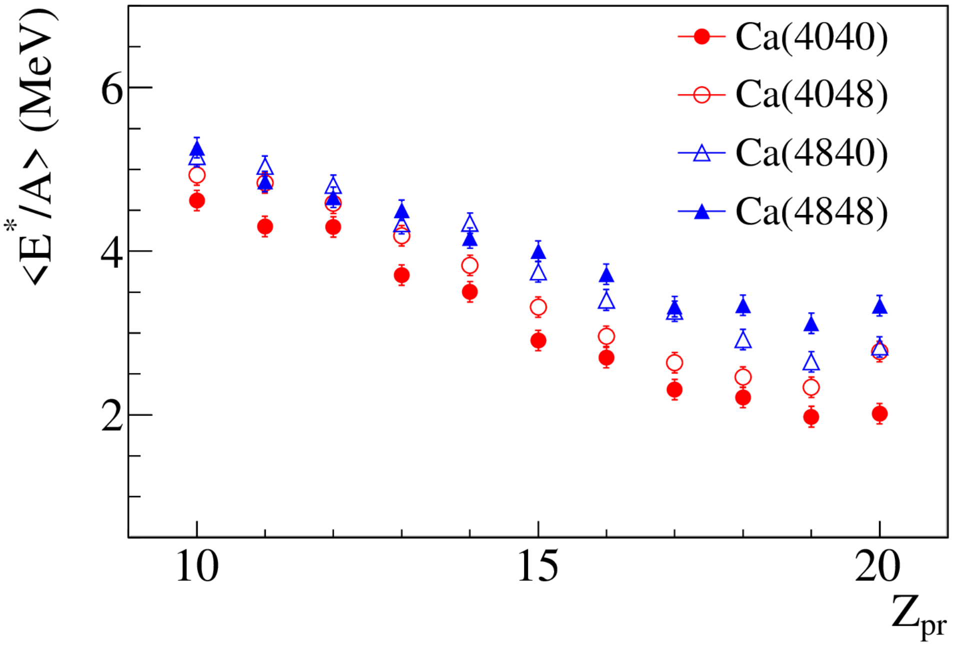

Figure 4.4: Average of the excitation energy per nucleon for the four systems under study. This values are calculated with the contribution of the evaporated neutrons, estimated by eq.(4.2).

system was in equilibrium), whereas a value of $n/z = 1.10$ is defined for the $^{40}Ca+^{48}Ca$ system.

Fig.(4.4) shows the excitation energy with an hypothesis on the number of evaporated neutrons as a function of the primary charge for the four different systems. We observe that neutron-rich systems, notably the $^{48}Ca+^{48}Ca$ system, have higher excitation energies than the neutron-poor systems. For crossed systems, we observed a significant memory of the projectile with a slight influence of the target.

4.3 Temperature

It is experimentally possible to estimate the temperature of an emitting source from the proton energy distributions. We hypothesize that sources emit according to Weisskopf's statistical evaporation model, where a surface emission is chosen [6]. In this context, the particles are emitted statistically by a thermalized core and their energy distribution will have a Maxwellian form. We must, therefore, assume that the source is in equilibrium. The relative probability of emitting a particle i with kinetic energy (E_k) is written thus:

$$P_i(E_k) = \frac{E_k - B_i^{Coul}}{T^2} \exp\left(-\frac{E_k - B_i^{Coul}}{T}\right) \qquad E_k \geqslant B_i^{Coul} \tag{4.3}$$

where the parameter B_i^{Coul} is the Coulomb barrier for emitting particle i from the excited nucleus. T is called *apparent Temperature*, because when we use this method return only an average estimation of the temperature along the decay chain.

We now present in fig.(4.5) the temperatures obtained for the different primary charges and for the four different systems. In the same way, as for the excitation energies, we observe a decrease in the temperature as one approaches the projectile charge. In addition, we observe that the temperatures for the ^{48}Ca projectile systems are higher than the temperatures for the ^{40}Ca projectile systems and with the increasing of the centrality, they reach almost the same temperature ($\sim 6.5\,MeV$).

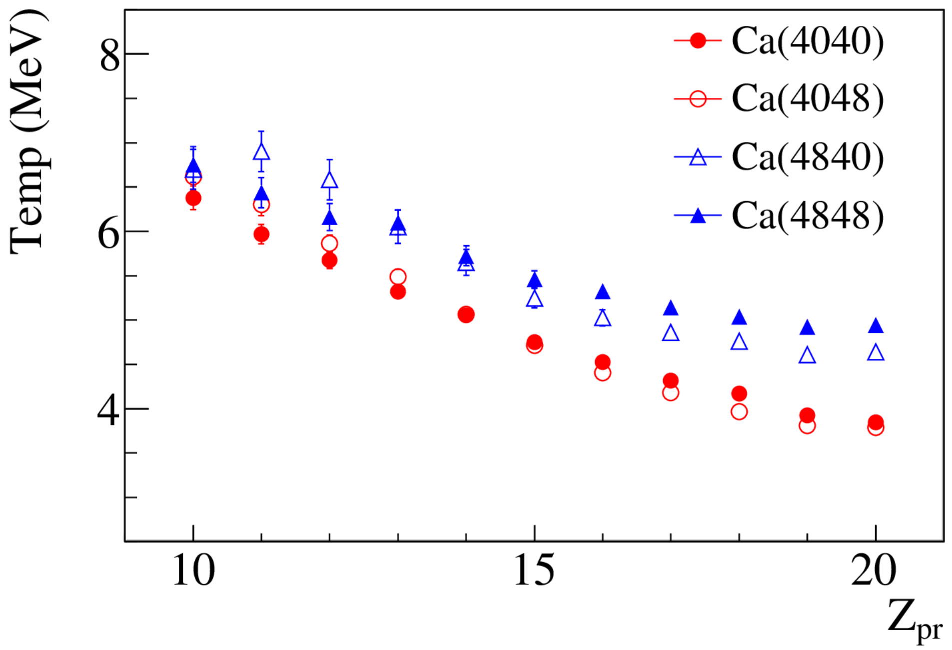

Figure 4.5: Temperature in function of the primary charge of the fragment for the different system under study.

4.4 Caloric curve

One of the possible thermodynamical signatures for a first order phase transition is a discontinuity in the heat capacity. Nuclear thermodynamics is based on nuclear calorimetry (measurement of the excitation energy, E^*) and nuclear thermometry (measurement of nuclear temperature, T). Nuclear temperatures are measured by determining the slopes of the kinetic energy distributions of evaporated light particles ('kinetic' temperatures), the ratio of the populations of discrete states for selected clusters ('excited state' temperature) or by the double-ratios of isotopic yields ('double-ratio' temperatures) [41]. These three methods have been used for a variety of systems in different collision regimes, some results are compiled in fig.(4.6). For a given method, data from different collaborations agree while the three methods do not give the same values.

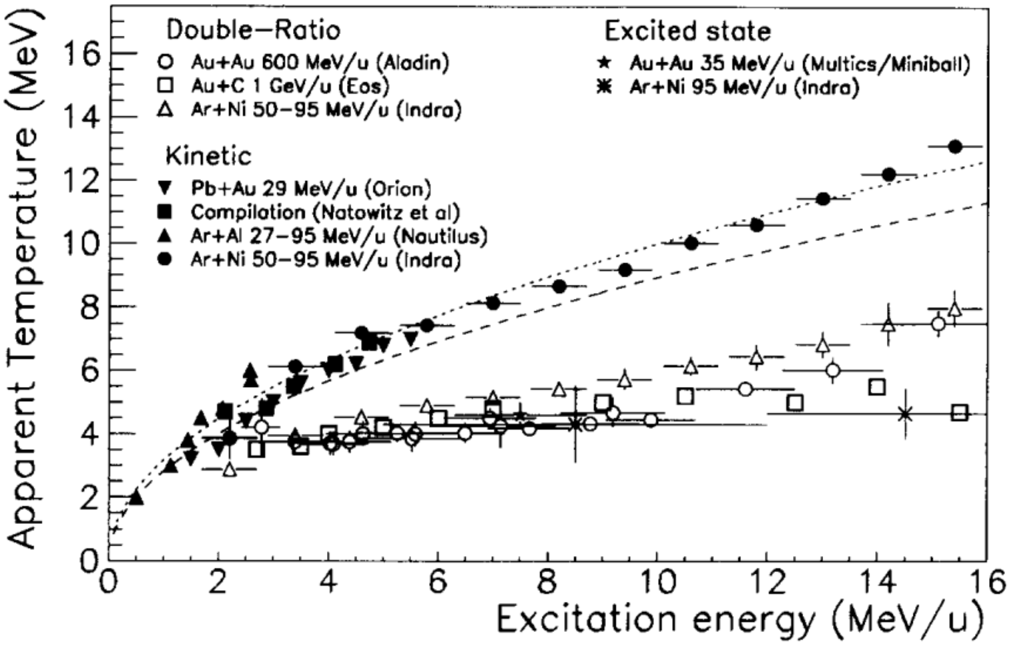

Figure 4.6: Systematics of measured nuclear temperatures with three diffent methods as a function of the excitation energy [6].

Consequently, it may be considered that only apparent temperatures are measured, as we already anticipate in the previous section. The 'kinetic' temperatures follow approximatively a Fermi gas law while the 'excited state' temperatures seem to saturate and the 'double ratio"s to slowly increase.

In fig.(4.7), we present the correlation between the excitation energy per nucleon (calculated in sec.(4.2)) and the 'kinetic' temperature (calculated in sec.(4.3)). This plot is called *caloric curve*. We can't afford to say something about the transition phase, because we don't see the plateau, what we can do is to consider the approximation where: the nucleus is described in a model of indipendent particles with a single-particle energy levels, and for moderate excitation energies, in this context the density state is written as

$$\rho(E, A) \simeq \frac{1}{\sqrt{48}E^*} e^{2\sqrt{aE^*}} \tag{4.4}$$

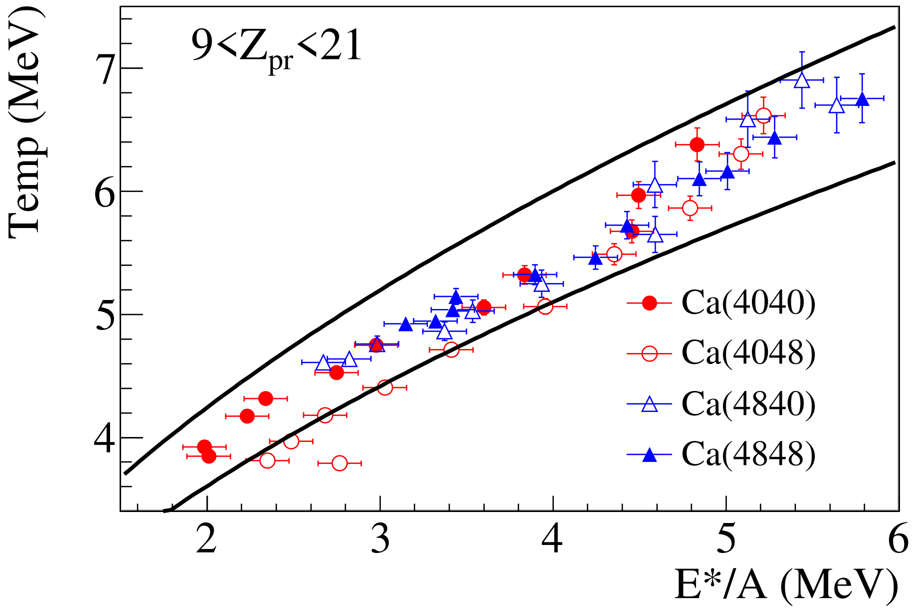

Figure 4.7: Nuclear 'kinetic' temperature as a function of the excitation energy per nucleon for the $9 < Z_{pr} < 21$ fragments. The two solid lines represent the constraints for the density level parameter, eq.(4.6).

where a is the *level density parameter*. At same level of approximation, one can link the excitation energy to the temperature:

$$E^*/A \simeq a \cdot T^2 \,. \tag{4.5}$$

We are interested in this relation because the density of state is a difficult object to evaluate. So we can give, only, some qualitative constraint to the density level parameter, that in fig.(4.7) are shown using the two solid lines that have the following equations:

$$\begin{aligned} T &= \sqrt{9 \cdot E^*/A} \\ T &= \sqrt{6.5 \cdot E^*/A} \,. \end{aligned} \tag{4.6}$$

4.5 Determination of the symmetry energy

In this section, we will present the preliminar results of the symmetry energy extract from the fit of the experimental isotopic distributions of the reconstructed primary fragments. We consider only the mass of the primary fragments without the contribution of the evaporated neutrons (what we called A_{prwon}). In order to avoid overloading the nomenclature, in the following, we will call it just A_{pr}. Fig.(4.8), shows the values of $K(N,Z)$ for $9 < Z_{pr} < 21$, represented by symbols, as a function of A_{pr}. The values are obtained by combining the results of the four systems $^{40,48}Ca +^{40,48} Ca$, according to the prescription of *A.Ono et al.* [24]. The curves for each Z was obtained by fitting $K(N,Z)$ using eq.(1.24).

The parameter $\zeta(Z)$ of the quadratic term in $(N-Z)$, in eq.(1.24), is equal to the sym-

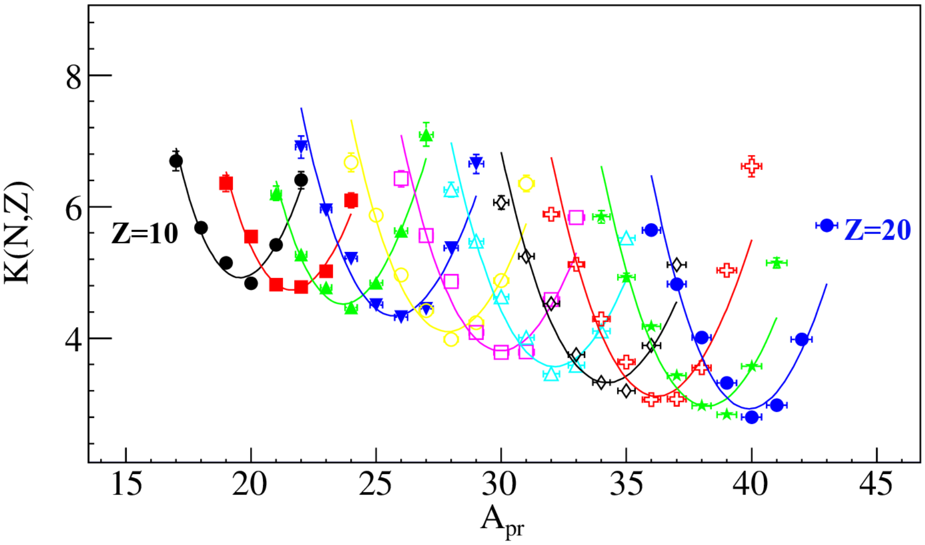

Figure 4.8: $K(N,Z)$ distribution for $9 < Z_{pr} < 21$ as a function of A_{pr}, using a combination of the 4 systems $^{40,48}Ca +^{40,48} Ca$. The curves for each Z was obtained by fitting $K(N,Z)$ using eq.(1.24).

metry energy divided by the temperature $\zeta = C_{sym}/T$, as demonstrated in ref. [24]. The values of ζ, resulting from the fit in fig.(4.8), are reported in fig.(4.9).

To obtain the C_{sym} value we have to multiply ζ by the temperature. We use the average value deduced from fig.(4.5), i.e. a global temperature for the four systems ($T \simeq 5.26\,MeV$). The results of the C_{sym} using this temperature are shown in fig.(4.10). In the figure is also added the parametrization of the symmetry energy for the ground state nuclei, calculated with AMD in ref. [24]:

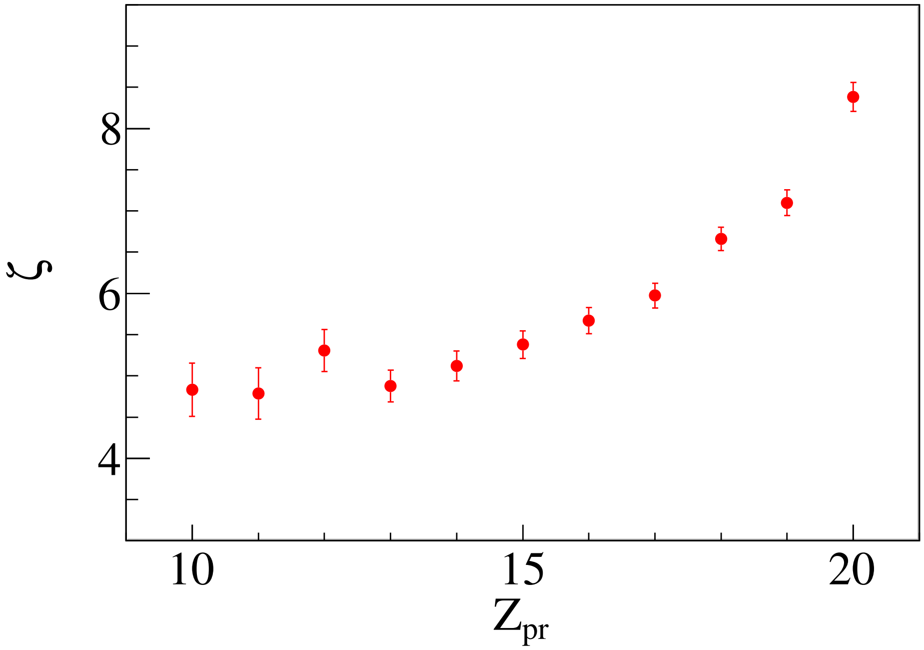

Figure 4.9: ζ values using a combination of the four systems ${}^{40,48}Ca + {}^{40,48}\,Ca$.

$$C_{sym}(A = 2Z) = c_v + c_s(2Z)^{-1/3} \tag{4.7}$$

where $c_v = 30.9\,MeV$ and $c_s = -35.2\,MeV$.

Our result of C_{sym} is higher than the parametrization for nuclei in the ground state. We have two possible interpretations of this observation:

i) The temperature extracted from the proton kinetic energy spectra is sensitive to the dynamical effects that can increase the slope. Consequently it increases the

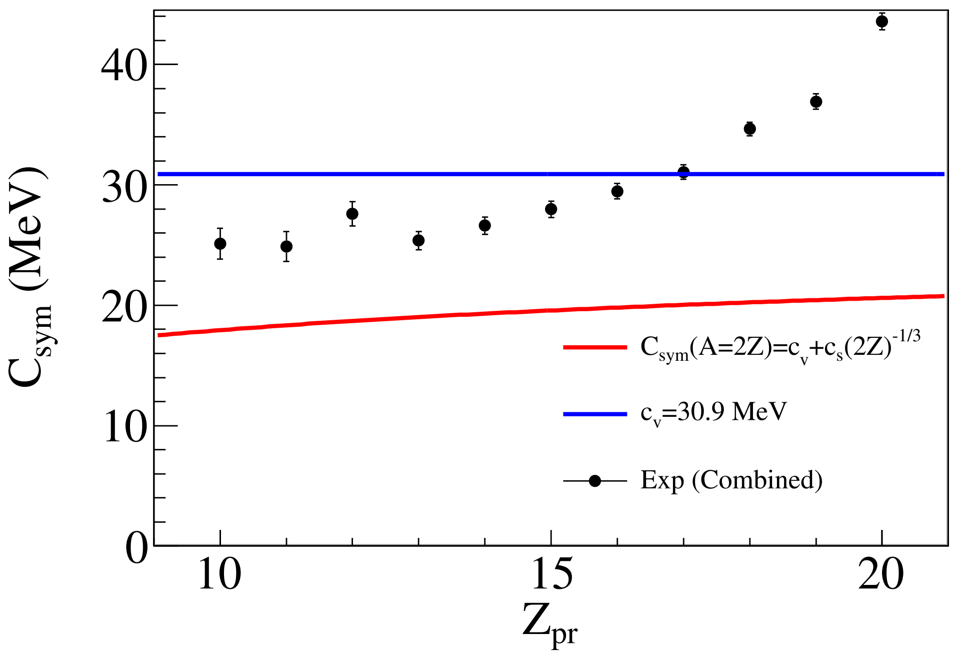

Figure 4.10: C_{sym} values using a combination of the 4 reactions as a function of the primary charge, calculate using the global temperature $T = 5.2\,MeV$. The red line shows the symmetry energy of a nucleus in its ground state. The blue line shows $c_v = 30.9\,MeV$.

apparent temperature and, therefore, the symmetry energy. Lowering the temperature for about 1 MeV can put our data points (C_{sym}) on the top of the parametrization up to $Z_{pr} = 16$. In this case the surface effects are important in the collisions we are explore ($-c_v/c_s = 1.14$). The system should explore the densities close to the saturation (ρ_0). This result corroborate the fact that the two interactions used in AMD gave almost the same results when trying to reproduce the data (see fig.(4.2)). In the case of $Z_{pr} \geq 17$, we observe an increase of the C_{sym}, this is probably due to a mixture of various reaction mechanisms. Indeed, in sec.(3.2) a detailed study of the fragments have shown an overlap of different transfer reactions.

ii) The second explanation is that our result is correct, in this case the increase of the observed C_{sym} is due to a larger volume which may reflects lower densities. This effect has been predicted by *Raduta et al.* [42] using MMM (*Microcanonical Multifragmentation Model*) calculations. The calculations predict an higher values of C_{sym} than the parametrization values when assuming a low density of the breaking system, see fig.(4.11).

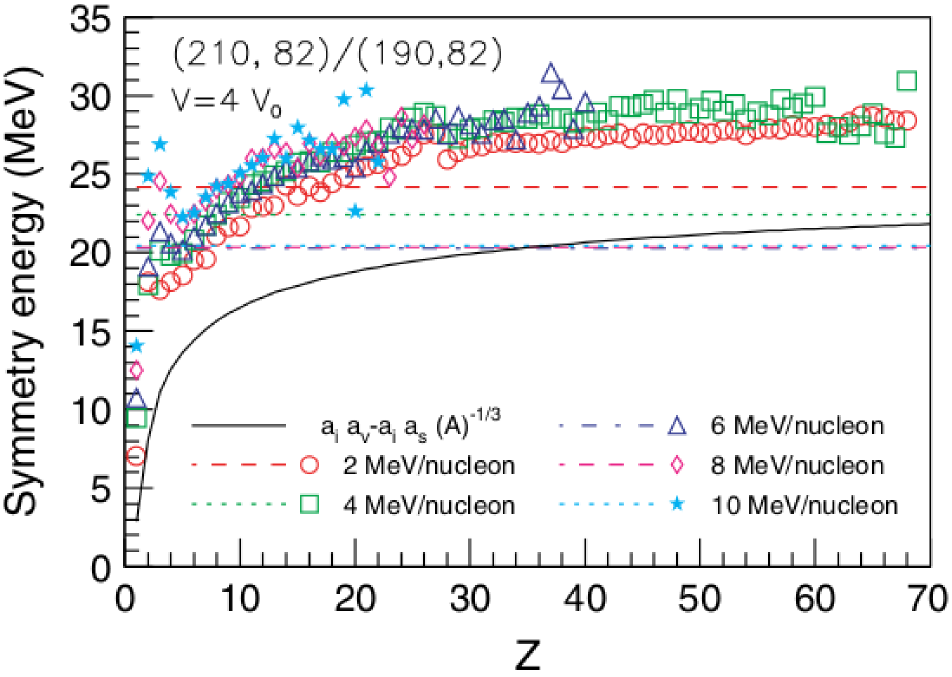

Figure 4.11: MMM predictions for the symmetry energy as a function of Z in the asymptotic stage of the decay as obtained using two different parametrizations, we are interested to the one represented by the simbols (for further details, see [42]). The equilibrated systems are (190, 82) and (210, 82) with $V = 4V_0$ (this means density lower than ρ_0) and excitation energies ranging from 2 to 10 MeV/u [42].

Chapter 5

Conclusions

In this thesis, we have underlined the importance of the heavy ion collision experiments for investigating nuclear systems at extreme conditions of density, temperature, and isospin. This allows to explore the density dependence of the nuclear equation of state and in particular, the symmetry energy term. We have shown that experimentally the symmetry energy affects the isotopic production. The observables sensitive to this term are the isoscaling, the isotopic distribution and the isospin transport (see sec.(1.3)).
A new generation detector apparatus, FAZIA, has been built in this physical context, with the aim of detecting and identifying, in charge and mass (Z, A), the reaction products in the widest range possible. A phase of research and development allowed to optimize the performance of silicon detectors by choosing appropriate material and by selecting the best ones. The apparatus is made of three stage telescopes $Si1-Si2-CsI(Tl)$ arranged in a way to have 16 telescope in a single module. In the present situation, it clearly discriminates charges up to $Z \sim 55$ and masses up to $Z \sim 25$. The techniques to identify the fragments stopped in different layers of FAZIA are implemented inside a C++ library called KaliVeda based on the ROOT analysis framework. The methods used are the $\Delta E - E$ technique and the Pulse shape analysis. The FAZIA apparatus was designed to be used with different detecting systems. The first coupling with INDRA apparatus has been performed at GANIL (2019). The reactions of the experiment INDRA-FAZIA (e709) are $^{58,64}Ni + ^{58,64}Ni$ in the energetic range $(35 - 50\, MeV/u)$. The

data will be calibrated before being analyzed. Since the calibration phase is a very long one and it is just started, during my internship at GANIL (21/01-31/05/2019), I have analyzed data of a previous INDRA-VAMOS campaign (*e503*) for the reactions $^{40,48}Ca +^{40,48} Ca$ at $35\, MeV/u$. The results of the analysis will be very useful for making comparisons between the two experiments. In the INDRA-FAZIA experiments, we expect a minor mass resolution but a larger angular coverage and the set-up is easier to be analyzed with respect to the experiment with VAMOS.

In these collisions, the transport models predict the formation of a low-density neck between two hot fragments kinematically similar to the projectile (*Projectile-Like Fragment*, PLF) and target (*Target-Like Fragment*, TLF). The spectrometer covers the forward polar angle from 2.5^o to 6.5^o, with an acceptance of $\theta \simeq \pm 2^o$, thus allowing the detection of PLF emitted slightly above the grazing angle of the projectile. The multi-detector INDRA covers the polar angle from 7^o to 176^o, thus allowing the detection of the *light charged particles* (LCP). In order to understand some of the various mechanisms involved during the reaction process, it is important to investigate the evolution of the average neutron excess ($< A > -2Z$) of the fragments detected in VAMOS as a function of their atomic number. In nuclear reactions, one or more excited primary fragments are formed which decay by evaporation of nucleons and light clusters. This evaporation process can substantially alter the proton-neutron asymmetry of the initial primary fragments. What was noted is that at sufficiently large excitation energies, independent of the assumed Z and A of the primary fragments, evaporation models predict that the average position of the secondary fragments in the chart of nuclides is always close to a particular line, the so-called evaporation attractor line (EAL).

Using the isotopic identification of PLF provided by VAMOS, together with those of LCP revealed in coincidence with INDRA allows, through their correlation, to reconstruct the primary fragment. The primary fragment charge (Z_{pr}) is reconstructed as the sum of the PLF charge and the evaporated LCP in the event, asking at least one particle in INDRA in coincidence with the fragment detected in VAMOS. In order to test the quality of the reconstruction, we studied the even-odd effect both for the PLF and for the primary fragment. We understand that this effect is due to the evaporation process and this is why is present only for the PLF, which is excited (see sec.(4.1)).

However, during the reconstruction phase, the mass number (A) is extracted without the emitted neutron contribution (what we called A_{prwon}), because these are not detected. Indeed, to be sure about this reconstruction we made a comparison with the simulations. The simulation required two steps: the first one is to simulate the reaction using dynamical calculation provided by a dynamical molecular model AMD removing only the evaporated neutrons, these are estimated with a statistical calculation provided by the statistical code GEMINI++. We obtained a good agreement, so we went further in the analysis and we extrapolated some observables such as the excitation energy and the temperature of the primary fragments. However, to determine the excitation energy it is necessary to estimate the neutron emitted during the decay phase. We consider the following relation that conserves the mass number of the reaction:

$$N_{evaporated} = Z_{pr}\left(1 + \frac{n}{z}\right) - A_{prwon} \tag{5.1}$$

where on average, n/z should reflect the N/Z of the system, which is also equivalent to that of the projectile or target. We observed that neutron-rich systems have higher excitation energies than the neutron-poor systems. For crossed systems, we observed a significant memory of the projectile with a slight influence of the targe. Then, the nuclear temperature are measured by determining the slopes of the kinetic energy distributions of the evaporated light particles, the so-called *kinetic* temperature. The same behaviour of the excitation energy was observed for the temperature. Making the correlation between these two observables, we are able to deduce the caloric curve and from this, we made some qualitative constraint to the density level parameter that are shown in fig.(4.7).

Finally, through the study of the isotopic distribution, we obtained a preliminary result of C_{sym} values as a function of the reconstructed primary charge. Our result is higher than the parametrization for nuclei in the ground state. We have two possible interpretations of this observation:

i) The temperature extracted from the proton kinetic energy spectra is sensitive to the dynamical effects that can increase the slope. Consequently it increases the apparent temperature and, therefore, the symmetry energy. Lowering the temperature for about 1 MeV can put our data points (C_{sym}) on the top of the parametrization up to $Z_{pr} = 16$. In this case the surface effects are important in the collisions we are explore ($-c_v/c_s = 1.14$). The system should explore the densities close to the saturation (ρ_0). This result corroborate the fact that the two interactions used in AMD gave almost the same results when trying to reproduce the data (see fig.(4.2)). In the case of $Z_{pr} \geq 17$, we observe an increase of the C_{sym}, this is probably due to a mixture of various reaction mechanisms. Indeed, in sec.(3.2) a detailed study of the fragments have shown an overlap of different transfer reactions.

ii) The second explanation is that our result is correct, in this case the increase of the observed C_{sym} is due to a larger volume which may reflects lower densities. This effect has been predicted by *Raduta et al.* [42] using MMM (*Microcanonical Multifragmentation Model*) calculations. The calculations predict an higher values of C_{sym} than the parametrization values when assuming a low density of the breaking system, see fig.(4.11).

We started working also on isotopic transport, i.e. the influence of target isospin in the QP, but we need to increase the statisticas of the simulations because the error bars don't allow us to make any comparison. Indeed, one of the next steps will be to work to improve the simulations, very time concerning computer code. Another important step is exploring the symmetry energy by considering the measurements of the properties of the clusters produced during the evolution of the system. Indeed, there are models considering the nuclei as formed with clusters instead of single nucleons. In particular, the IKEDA diagram [43] predicts $\alpha - clusters$ pre-formation in even-even nuclei. The diagram has been extended also to other nuclei where neutrons can be the glue to take together $\alpha - clusters$ [44]. In this respect, it could be interesting to investigate how at low density, uniform nuclear material becomes unstable with respect to clustering. At densities lower than the saturation density, the inter-nucleon separation becomes comparable to the nucleon-nucleon interaction, so that it becomes energetically favorable for the system to fragment into neutron-rich clusters. Clustering significantly increases symmetry energy at very low densities, which could be useful also for modeling the explosion of Core-Collapse Supernovae Type II.

Bibliography

[1] G.R. Satchler. *Introduction to Nuclear Reactions*. Palgrave Macmillan, 1990.

[2] R. Kaufmann and R.Wolfgang. Nucleon transfer reactions in grazing collisions of heavy ions. *Phys. Rev. Lett.*, 121:192–205, Jan 1961.

[3] W.U. Schröder, J.R. Birkelund, J.R. Huizenga, K.L. Wolf, and V.E. Viola. Mechanisms of very heavy-ion collisions : The 209bi + 136xe reaction at elab = 1130 mev. *Physics Report*, 45:301 – 343, 1978.

[4] W. Reisdorf. Flow particle yields equilibration in heavy ion reactions between 0.1 and 2 agev. *Nuclear Physics A*, 630(1):15–26, 1998.

[5] Hauger J.A. Albergo S. et al. Dynamics of the multifragmentation of 1 agev gold on carbon. *Phys. Rev. Lett.*, 77:235–238, Jul 1996.

[6] E. Suraud D. Durand and B. Tamain. *Nuclear dynamics in the nucleonic regime*. Institute of Physiscs Publishing, 2001.

[7] M.F. Rivet. B. Borderie. Nuclear multifragmentation and phase transition for hot nuclei. progress in particle and nuclear physics. *Elsevier*, pages pp.551–601, 2008.

[8] D. Gruyer, J. D. Frankland, E. Bonnet, A. Chbihi, G. Ademard, M. Boisjoli, and Borderie et al. Coulomb chronometry to probe the decay mechanism of hot nuclei. *Phys. Rev. C*, 92:064606, Dec 2015.

[9] M. D'Agostino, G. J. Kunde, P. M. Milazzo, J. D. Diniu, M. Bruno, and Colonna et al. Multifragmentation in e/a=35 mev collisions: Evidence for a coulomb driven breakup? *Phys. Rev. Lett.*, 75:4373–4376, Dec 1995.

[10] M D'Agostino, A Botvina, P.M. Milazzo, Mauro Bruno, Gerd Kunde, D.R. Bowman, and L et al Celano. Statistical multifragmentation in central au + au collisions at 35 mev/u. *Physics Letters B*, 371:175–180, 12 1995.

[11] Pawel Danielewicz and Jenny Lee. Symmetry Energy I: Semi-Infinite Matter. *Nucl. Phys.*, A818:36–96, 2009.

[12] Lie-Wen Chen, Che Ming Ko, Bao-An Li, Chang Xu, and Jun Xu. Probing isospin- and momentum-dependent nuclear effective interactions in neutron-rich matter. *The European Physical Journal A*, 50, 10 2013.

[13] X. Vinas, M. Centelles, X. Roca-Maza, and M. Warda. Density dependence of the symmetry energy from neutron skin thickness in finite nuclei. *Eur. Phys. J. A*, 50(2):27, 2014.

[14] M Toro, Virgil Baran, M Colonna, and Vincenzo Greco. Topical review: Probing the nuclear symmetry energy with heavy-ion collisions. *Journal of Physics G-nuclear and Particle Physics - J PHYS G-NUCL PARTICLE PHYS*, 37, 08 2010.

[15] G. Ademard et al. Isospin effects and symmetry energy studies with INDRA. *Eur. Phys. J.*, A50:33, 2014.

[16] M. B. Tsang, W. G. Lynch, H. Xi, and W. A. Friedman. Nuclear thermometers from isotope yield ratios. *Phys. Rev. Lett.*, 78:3836–3839, May 1997.

[17] M. B. Tsang, W. A. Friedman, C. K. Gelbke, W. G. Lynch, G. Verde, and H. S. Xu. Isotopic scaling in nuclear reactions. *Phys. Rev. Lett.*, 86:5023–5026, May 2001.

[18] Akira Ono, P. Danielewicz, W. A. Friedman, W. G. Lynch, and M. B. Tsang. Isospin fractionation and isoscaling in dynamical simulations of nuclear collisions. *Phys. Rev. C*, 68:051601, Nov 2003.

[19] V. Baran, M. Colonna, M. Di Toro, M. Zielinska-Pfabé, and H. H. Wolter. Isospin transport at fermi energies. *Phys. Rev. C*, 72:064620, Dec 2005.

[20] V. Baran, M. Colonna, V. Greco, and M. Di Toro. Reaction dynamics with exotic beams. *Phys. Rept.*, 410:335–466, 2005.

[21] H. A. Bethe and R. F. Bacher. Nuclear physics a. stationary states of nuclei. *Rev. Mod. Phys.*, 8:82–229, Apr 1936.

[22] G. Gamow. Mass defect curve and nuclear constitution. *Proc.R. Soc. Lond*, 803:632–644, 1930.

[23] E. Geraci, M. Bruno, M. D'Agostino, E. De Filippo, A. Pagano, and G. Vannini et al. Isoscaling in central 124sn+64ni, 112sn+58ni collisions at 35 amev. *Nuclear Physics A*, 732:173 – 201, 2004.

[24] Akira Ono, P. Danielewicz, W. A. Friedman, W. G. Lynch, and M. B. Tsang. Symmetry energy for fragmentation in dynamical nuclear collisions. *Phys. Rev. C*, 70:041604, Oct 2004.

[25] Fazia collaboration. `http://fazia.in2p3.fr/?lang=en`.

[26] Remi Bougault, G Poggi, S Barlini, Bernard Borderie, Giovanni Casini, Abdou Chbihi, and N et al. Le Neindre. The fazia project in europe: *r&d* phase. *European Physical Journal A*, 50, 02 2014.

[27] S. Valdré, G. Casini, N. Le Neindre, M. Bini, A. Boiano, and B. Borderie et al. The fazia setup: A review on the electronics and the mechanical mounting. *Nuclear Instruments and Methods in Physics Research Section A: Accelerators, Spectrometers, Detectors and Associated Equipment*, 930:27 – 36, 2019.

[28] G. F. Knoll. *Radiation Detction and Measurement*. 1999.

[29] J. Pouthas et al. Indra, a 4π charged product detection array at ganil. *Nuclear Instruments and Methods in Physics Research Section A : Accelerators, Spectrometers, Detectors and Associated Equipment*, 357(220133):418 – 442, 1995.

[30] J. Pouthas et al. The electronics of the indra 4π detection array. *Nuclear Instruments and Methods in Physics Research Section A : Accelerators, Spectrometers, Detectors and Associated Equipment*, 369(1):222 – 247, 1996.

[31] Maxime Henri. *Study of the transport and equilibration properties of the nuclear matter in the Fermi energy domain*. Theses, Université Caen Normandie, Oct 2018.

[32] Kaliveda:toolkit for analysis & simulation of fermi energy heavy-ion collisions. `http://indra.in2p3.fr/kaliveda/`.

[33] Root: A data analysis framework. `https://root.cern.ch/`.

[34] W. R. Leo. *Techniques for Nuclear and Particle Physics Experiments: A How to Approach*. 1987.

[35] Diego D. Gruyer. *Dynamic aspects of the nuclear decay : from the fission to the multifragmentation*. Theses, Universitè de Caen-Basse Normandie, September 2014.

[36] J. Lukasik, J. Benlliure, V. Métivier, E. Plagnol, B. Tamain, M. Assenard, G. Auger, Ch. O. Bacri, E. Bisquer, B. Borderie, R. Bougault, R. Brou, Ph. Buchet, J. L. Charvet, A. Chbihi, and alt. Dynamical effects and intermediate mass fragment production in peripheral and semicentral collisions of xe+sn at 50 mev/nucleon. *Phys. Rev. C*, 55:1906–1916, Apr 1997.

[37] R J. Charity. N-z distributions of secondary fragments and the evaporation attractor line. *Physical Review, C*, 58, 08 1998.

[38] G. Casini, S. Piantelli, P. R. Maurenzig, A. Olmi, L. Bardelli, S. Barlini, M. Benelli, M. Bini, M. Calviani, and P. et al. Marini. Persistence of odd-even staggering in charged-fragment yields from ^{112}sn + ^{58}ni collisions at 35 mev/nucleon. *Phys. Rev. C*, 86:011602, Jul 2012.

[39] Yoshiko Kanada-En'yo, Masaaki Kimura, and Akira Ono. Antisymmetrized molecular dynamics and its applications to cluster phenomena. *PTEP*, 2012:01A202, 2012.

[40] R.J. Charity. Gemini: A code to simulate the decay of a compound nucleus by a series of binary decays. *Joint ICTP-IAEA Advanced Workshop on Model Codes for Spallation Reactions*, 01 2008.

[41] Dominique Durand. Nuclear matter from nuclear collisions. *Nuclear Physics A*, 654(1):C273 – C293, 1999. Proceedings of the International Nuclear Physics Conference.

[42] Ad. R. Raduta and F. Gulminelli. Multifragmentation and the symmetry term of the nuclear equation of state. *Phys. Rev. C*, 75:024605, Feb 2007.

[43] Kiyomi Ikeda, Noboru Takigawa, and Hisashi Horiuchi. The Systematic Structure-Change into the Molecule-like Structures in the Self-Conjugate 4n Nuclei. *Progress of Theoretical Physics Supplement*, E68:464–475, 07 1968.

[44] W. von Oertzen. Covalently bound molecular structures in the $\alpha +^{16} o$ system. *Eur. Phys. J. A*, 11(4):403–411, 2001.

List of Figures